




Article

Investigation of the Electrochemical Behaviour of Al Current Collector Material Polarised Highly Anodically and Located in Butyltrimethylammonium Bis(trifluoromethylsulfonyl)imide Room-Temperature Ionic Liquid

Jaanus Kruusma ¹, Tanel Käämbre ², Arvo Tõnisoo ², Vambola Kisand ², Karmen Lust ¹ and Enn Lust ^{1,*}¹ Institute of Chemistry, University of Tartu, Ravila 14a, 50411 Tartu, Estonia; jaanus.kruusma@ut.ee (J.K.)² Institute of Physics, University of Tartu, W. Ostwaldi 1, 50411 Tartu, Estonia

* Correspondence: enn.lust@ut.ee; Tel.: +372-737-5165; Fax: +372-737-5264

Abstract: The electrochemical behaviour of Al, used as a current collector in supercapacitors and in Li-ion and Na-ion electrochemical power sources, was investigated for the first time using the in situ soft X-ray photoelectron spectroscopy (XPS) method, collecting the information directly at the electrolyte-covered Al current collector polarised electrochemically at high anodic potentials. Cyclic voltammetry, electrochemical impedance spectroscopy, and synchrotron in situ soft XPS methods were applied to collect physical and electrochemical information characterising the electrochemically polarised Al-current-collector RTIL interface soaked into the butyltrimethylammonium bis(trifluoromethylsulfonyl)imide (N4111(TFSI)) room-temperature ionic liquid. The obtained data show the start of intensive oxidation processes, including aluminium oxidation and the formation of an insoluble Al(TFSI)₃ surface layer in N4111(TFSI) at $E \geq 3.0$ V (vs. Ag-QRE). Very intensive electro-oxidation of TFSI⁻ anions at $E \geq 6.5$ V (vs. Ag-QRE) has been observed. CV data indicate that the electrochemical oxidation of once-activated Al is possible in N4111(TFSI) at $1.1 \text{ V} < E < 1.6 \text{ V}$ (vs. Ag-QRE). Therefore, the oxidation of Al starts at $E \geq 2.05$ V (vs. Ag-QRE) if the Al surface is modified with electro-oxidation products of TFSI⁻ anions.

Keywords: aluminium current collector; room-temperature ionic liquid; in situ X-ray photoelectron spectroscopy; electrochemical impedance spectroscopy; cyclic voltammetry



Citation: Kruusma, J.; Käämbre, T.; Tõnisoo, A.; Kisand, V.; Lust, K.; Lust, E. Investigation of the Electrochemical Behaviour of Al Current Collector Material Polarised Highly Anodically and Located in Butyltrimethylammonium Bis(trifluoromethylsulfonyl)imide Room-Temperature Ionic Liquid. *Batteries* **2023**, *9*, 189. <https://doi.org/10.3390/batteries9030189>

Academic Editor: Xiaohui Song

Received: 9 February 2023

Revised: 13 March 2023

Accepted: 17 March 2023

Published: 22 March 2023



Copyright: © 2023 by the authors. Licensee MDPI, Basel, Switzerland. This article is an open access article distributed under the terms and conditions of the Creative Commons Attribution (CC BY) license (<https://creativecommons.org/licenses/by/4.0/>).

1. Introduction

Butyltrimethyl ammonium bis (trifluoromethylsulfonyl) imide (N4111(TFSI), CAS number 258273-75-5), is one of the quaternary ammonium-based room-temperature ionic liquids (RTILs) being suggested to use as an electrolyte in supercapacitors and electrochemical power sources due to its very wide region of ideal polarizability at the carbon electrode–electrolyte interface [1,2]. However, it has been reported that aluminium, which is used as a current collector in many electrochemical applications [3–6], can corrode intensively in the N4111(TFSI) environment [4,7,8].

It is known that Al-current-collector passivation depends on the availability of F⁻ ions, as previous XPS surface analysis has shown the presence of a thin layer of insoluble AlF₃ on the surface of the passivated Al current collector [9–11]. On the other hand, a thick pore-free Al₂O₃ layer on top of pure Al or its alloys has also been found to be an excellent corrosion inhibitor [12–14]. This kind of non-porous protecting Al₂O₃ layers is also essential to produce high-voltage electrolytic-capacitor electrodes [15,16] and high-voltage electrochemical power-source current collectors [17–19] or to obtain corrosion-resistant unpainted Al-based consumables [20,21]. To form dense Al₂O₃ layers on Al or its alloys, Al materials must be anodised at very high voltages in aqueous [16] or inorganic (incl. RTIL) [14,22] electrolytes. In the anodisation process of Al in RTILs, it has been found that

both the chemical composition of RTIL anion and the concentration of water in the RTIL are very important factors influencing the quality of the formed Al_2O_3 thin film [14].

Additionally, the influence of RTIL anion size and other physical properties on the quality of the in operando formed AlF_3 film on the Al current collector of Li-ion or Na-ion power sources cannot be neglected, since it has been found that bis(perfluoroethylsulfonyl)imide anions [7] and fluorosulfonylimide anions [8] inhibit Al corrosion better than TFSI[−] anions in organic carbonate solutions [7,8]. On the other hand, corrosion of polarised Al current collectors is suppressed in the presence of TFSI[−] anions when pure RTILs are used instead of organic carbonate solutions [23]. Therefore, it is supposed that $\text{Al}(\text{TFSI})_3$ formed at the Al | RTIL interface at ca. $E = 3.7$ V vs. Li^+/Li is also insoluble in pure RTILs [4,9,23,24], as is the AlF_3 film [5,6,22,25,26]. This suggests the possibility of the construction of high-potential supercapacitors with a cell potential higher than 3.5 V, as proposed for *N*-butyl-*N*-methylpyrrolidinium TFSI and *N*-butyl-*N*-methylpyrrolidinium bis(fluorosulfonyl)imide RTILs [27,28].

The possibility of the electrochemical polishing of Al in RTILs is also intriguing. Hou et al. [29,30] electropolished Al in trimethylammonium aluminium tetrachloride at 50 °C, and Kityk et al. [31] found that Al can be anodically electropolished in the eutectic blend of choline chloride and ethylene glycol at room temperature by applying moderately low anodic potentials. Both workgroups also found that electrochemically polished Al surfaces are more corrosion resistant due to the formation of a fresh, smooth, and compact Al_2O_3 protective surface film. Therefore, since N4111(TFSI), choline chloride, and trimethylammonium aluminium tetrachloride all contain organic ammonium cations, it was exciting to study the behaviour of Al in N4111(TFSI) at high anodic potentials from the point of possible aluminium electrochemical polishing.

Due to an insufficient amount of information about the stability of the Al current collector in the TFSI[−] anion containing neat RTIL, the electrochemical and adsorption behaviour of the N4111(TFSI) at the polarised Al surface at various fixed high positive potentials has been studied for the first time using synchrotron-initiated soft (i.e., low-energy) XPS and electrochemical methods. On the other hand, due to the large interest in the use of quaternary ammonium cation and TFSI[−] anions containing RTILs for the construction of high-voltage electrochemical energy sources and storage systems, and the technical importance of the anodisation of Al surfaces using RTILs containing some water, detailed analyses have been conducted. With the assistance of the low-energy in situ XPS method, the detected core electrons' binding-energy behaviour of N4111(TFSI) for the Al/ Al_2O_3 surface polarised at various potentials provided indirect information about the formation potential and the stability of the proposed $\text{Al}(\text{TFSI})_3$ film. It should be mentioned that the use of surface-sensitive XPS methods, especially those with low tuneable excitation energy, for the investigation of electrochemically polarised surfaces in situ is still not common and the experimental operando data are quite rare. Therefore, in addition to in situ XPS measurements, the CV and potentiostatic EIS methods were employed in parallel to obtain overwhelming electrochemical information.

2. Experiment

2.1. Materials

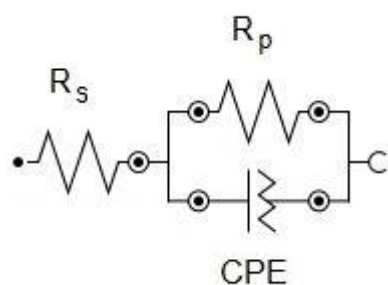
The same Al material was used in the following studies, as it was previously described and employed as the current collector in the model electrochemical double-layer capacitor containing molybdenum carbide-derived high-surface-area micro-mesoporous carbon electrodes [32,33]. Before the experiments, the Al material was first mechanically cleaned and polished with Carbimet[®] (SiC) 600 grit polishing paper (Buehler, 41 Waukegan Road, Lake Bluff, IL 60044, USA) and then washed with acetone (for HPLC, $\geq 99.8\%$, Honeywell/Riedel-de Haen, Charlotte, NC, USA). The purity of the pre-cleaned Al current collector was estimated by X-ray fluorescence spectroscopy, and it indicated the presence of 96.4% (*w/w*) Al, 1.9% (*w/w*) C and 1.7% (*w/w*) O at the mechanically treated material surface. Platinum gauze (with an apparent area of ca. 2 cm² and grid size of 100 mesh,

purity 99.9% (*w/w*)) as the counter electrode (CE) and a silver wire as the quasi-reference electrode (Ag-QRE) were located in the RTIL investigated.

N4111(TFSI) (>99.5%, IoLiTec Ionic Liquids Technologies GmbH, Zukunftspark 9, D-74076 Heilbronn, Deutschland) containing 80 ppm water and less than 50 ppm halides (according to the manufacturer's certificate) was further dried at 373 K and the pressure was reduced (10 kPa). Before in situ XPS measurement, the completed electrochemical cell containing the RTIL and all electrodes were degassed for 12 h at 295 K and $p = 5 \times 10^{-5}$ Pa before in situ XPS measurements.

2.2. Equipment and Data Analysis

The CV and EIS studies of the Al|N4111(TFSI) interface were performed in an mBraun Ar-filled glovebox ($p = 101$ kPa, 293 K) containing less than 0.1 ppm water and oxygen. A reference 3000 potentiostat (Gamry Instruments, 734 Louis Drive, Warminster, PA 18974, USA) was used to record electrochemical data and to polarise the Al electrode during the in situ XPS and MS measurements. The values of the series and parallel resistivities were calculated using the impedance spectra-fitting process by applying a model scheme containing the resistor in series with the parallel combination of resistor and constant-phase element (Scheme 1). Autolab NOVA 1.11 (Metrohm AG, Ionenstrasse 9100 Herisau, Switzerland) software was used for the calculation of theoretical spectra and fitting of the theoretical data to the experimental EIS.



Scheme 1. The equivalent scheme (model) used to describe the electrochemical behaviour of the N4111(TFSI)|Al interface. R_s —series resistance, R_p —parallel resistance, and CPE—constant-phase element.

The in situ XPS measurements were conducted in high-vacuum ($p = 0.5 \dots 5 \times 10^{-5}$ Pa) conditions in a synchrotron-initiated adjustable-energy X-ray beamline FinEstBeAMS using its gas-phase experiment end-station (Max IV laboratory, Lund University, Fotongatan 2, Sweden). Design of the synchrotron radiation beamline has been described in detail previously [34]. The following excitation-photon energies were used: for C 1s—400.0 eV, for N 1s—500.0 eV, for O 1s—650.0 eV, for F 1s—800.0 eV, and for S 2p and Al 2p—270 eV. Detailed XPS data analysis and binding-energy (*BE*) spectra fitting were performed using CasaXPS software (ver. 2.3.19, Casa Software Ltd., Bay House, 5 Grosvenor Terrace, Teignmouth, Devon, TQ14 8NE, UK). The C 1s XPS spectra were fitted using a combined Gaussian–Lorentz function with the ratio 70:30, respectively. For the calibration of the *BE* scale, the *BE* for the C 1s electrons originating from the aliphatic carbon atoms in the butyl chain (i.e., not connected with the ammonium-nitrogen atom and having an sp^3 electronic configuration) of the N4111⁺ cation located at the non-polarised Al WE was fixed at 285.0 eV [35]. This method enabled the calibration of the measured XPS spectra internally. For the precise fitting and extraction of the C 1s *BE* peaks, a two-peak model was selected for the analysis of the N4111⁺ cation core-electron energies.

The N 1s, O 1s, F 1s, and S 2p X-ray photoelectron (PE) spectra were fitted using the same combination ratio of the Gaussian–Lorentz function as described for C 1s XPS, leaving the FWHM and peak positions free. Later, the obtained individual peak *BE*s were corrected according to the *BE* for the aliphatic carbon, measured at different fixed potentials. All investigations were performed at room temperature (295 K).

3. Results and Discussion

3.1. In Situ XPS Measurements

To our knowledge, no data about Al current collector material covered with RTIL and polarised anodically (i.e., positively) and investigated in situ using the soft XPS method have been published so far. In situ soft XPS investigation results characterising an Al current collector covered also with N4111(TFSI) but polarised cathodically (i.e., negatively) were published recently [36].

The shapes of the C 1s, N 1s, O 1s, F 1s, and S 2p XPS spectra collected at a positively polarised Al current collector covered with N4111(TFSI) were stable within the potential (E) range from 0.00 V to 11.0 V (Figure 1a–e). It is important to note that no Al 2p signal was observed at the RTIL | vacuum interface within the potential range explored. This confirms that if the Al^{3+} -containing substances formed at the Al | N4111(TFSI) interface during Al oxidation they did not dissolve in N4111(TFSI). Additionally, the N4111(TFSI) layer at the Al/ Al_2O_3 electrode was thick enough and therefore no photoelectrons were detected from a clean Al surface or from its compounds (i.e., Al_2O_3 , AlF_3 , and $\text{Al}(\text{TFSI})_3$) formed and located at the N4111(TFSI) | Al interface (i.e., forming the Al electro-oxidation resisting layer, i.e., solid-electrolyte interface—SEI).

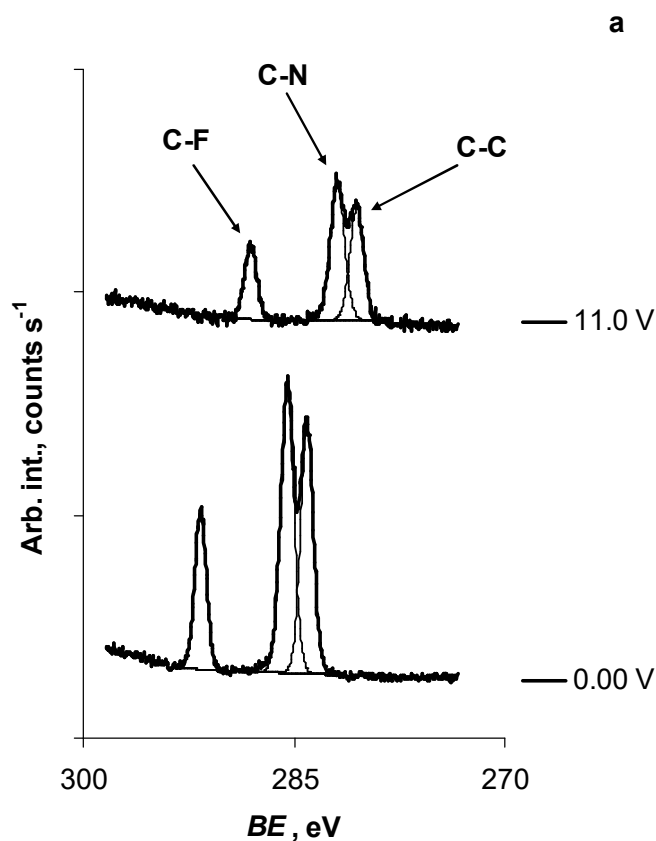


Figure 1. Cont.

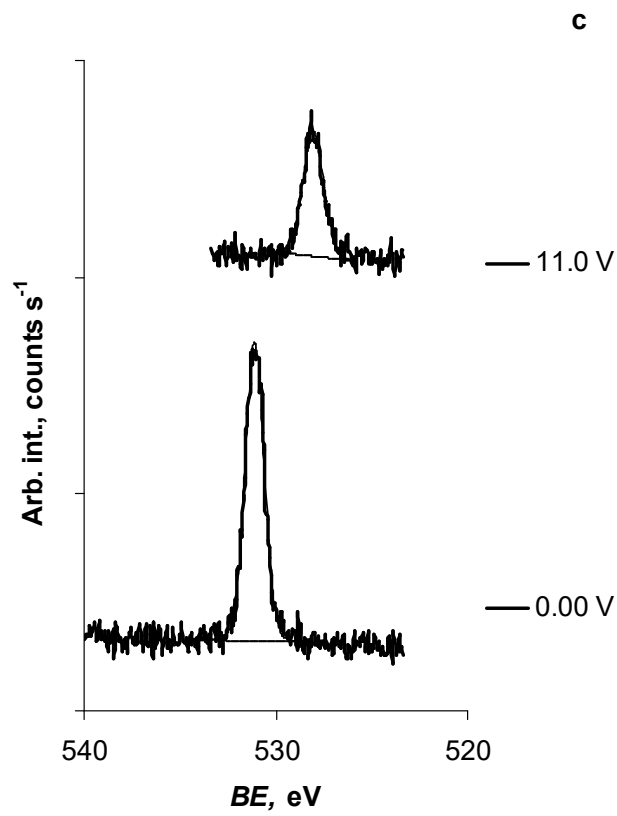
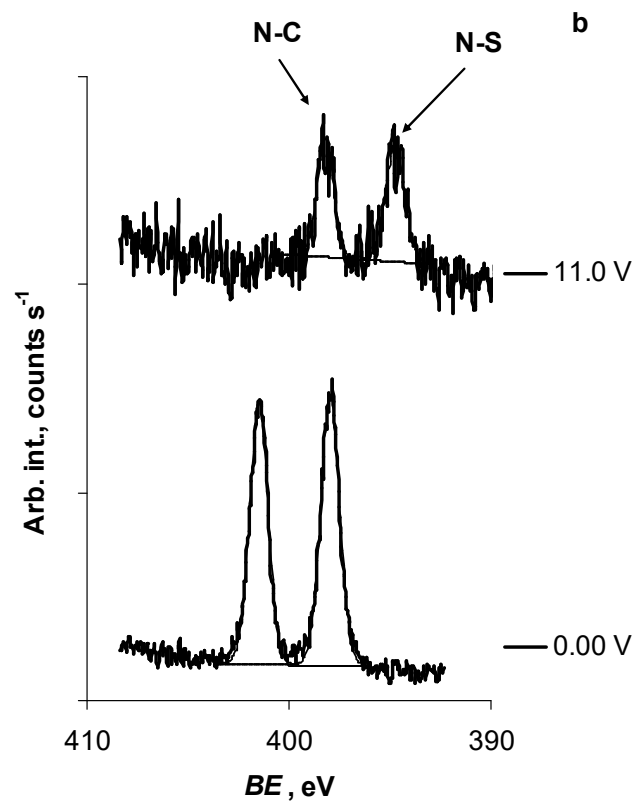


Figure 1. Cont.

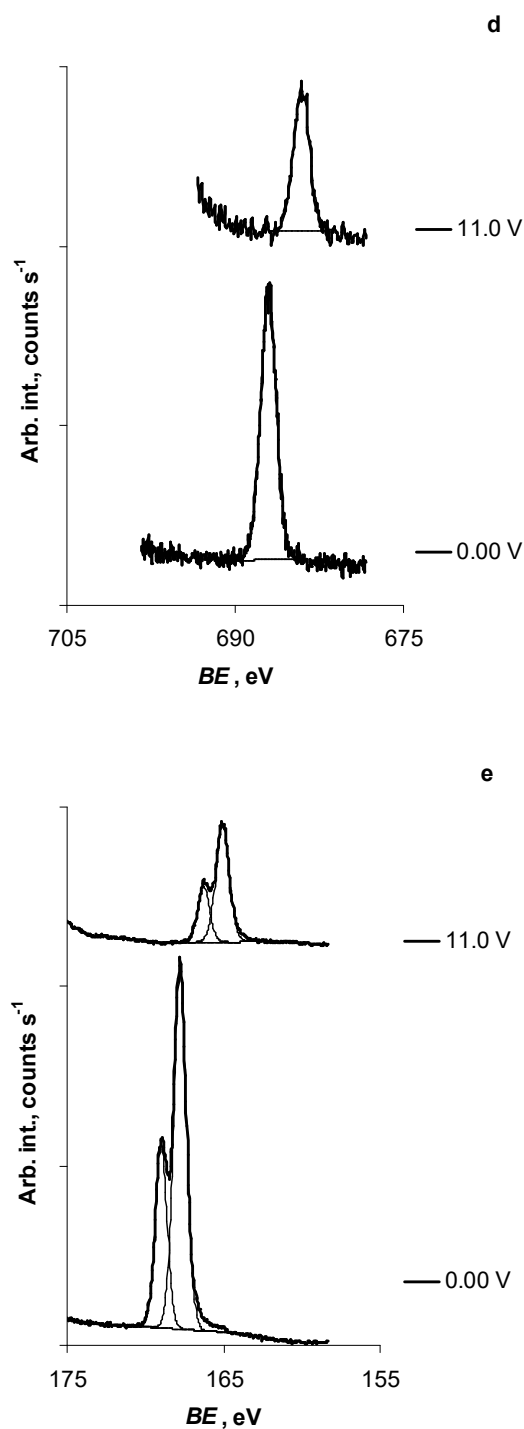


Figure 1. In situ XPS (i.e., core-electron binding energy, BE) data measured at variable Al-electrode potentials (marked in figures) for C 1s, tick mark labels 100 counts s^{-1} (a); for N 1s, tick mark labels 20 counts s^{-1} (b); for O 1s, tick mark labels 30 counts s^{-1} (c); for F 1s, tick mark labels 40 counts s^{-1} (d); and for S 2p, tick mark labels 400 counts s^{-1} (e).

However, the slopes of the BE vs. E relationships for C 1s, N 1s, O 1s, F 1s, and S 2p in situ XPS signals collected at the N4111(TFSI) | vacuum interface anodically polarised Al-current-collector surface were very interesting (Table 1 and Supplementary information Figure S1a–i). For all elements investigated within the potential range from 0.00 V to 3.00 V, the values of $dBE dE^{-1} = -0.82 \dots -0.86 \text{ eV V}^{-1}$, thus, being very close to the value -1.0 eV V^{-1} , indicating the non-specific adsorption [37,38] of N4111(TFSI) on the

Al/Al₂O₃ surface. At more positive potentials, i.e., for region from 3.00 V to 4.50 V, the values of $dBE dE^{-1}$ were close to zero (0.09 ... 0.14 eV V⁻¹), indicating very strong adsorption of N4111(TFSI) at the Al/Al₂O₃ surface (i.e., a surface-compound formation between N4111(TFSI) and Al/Al₂O₃) [37,38] at $E \geq 3.00$ V. No gas-bubble formation was noted at the Al/Al₂O₃ electrode covered with N4111(TFSI) in the potential range of $3.0 \text{ V} < E < 4.5 \text{ V}$; thus, we suppose that N4111⁺ or TFSI⁻ did not electro-oxidise and decompose. Zhou et al. [38], investigating the adsorption of 4,4'-dithiodipyridine (PySSPy) at Au(111), noted that BE of S 2p_{3/2} electrons did not change at the potentials where the strong adsorption of PySSPy had taken place. Although the core-electron BE of the other elements composing PySSPy changed by -0.9 eV V^{-1} , they concluded that the sulphur located in PySSPy adsorbed at the Au(111) electrode and formed a bond with Au. Based on that study [38] and the information collected in this study by the in situ XPS method for the N4111(TFSI) | Al interface, we suppose that the TFSI⁻ anion adsorbed strongly at the Al/Al₂O₃ surface or even reacted with the Al³⁺ cations formed. Although dBE vs. dE was nearly zero for the inner core electrons for the elements composing the N4111⁺ cation, we suppose that N4111⁺ remained somehow attached to the TFSI⁻ anion combined with the Al/Al₂O₃ or Al³⁺ cations.

Table 1. Core-electron binding energy vs. Al electrode potential relationships for various Al-electrode potential ranges measured with in situ X-ray photoelectron spectroscopy.

	0.00 V < E < 3.00 V	3.00 V < E < 4.50 V	8.50 V < E < 11.00 V
C 1s, C-N	-0.82 eV V^{-1}	0.15 eV V^{-1}	-0.89 eV V^{-1}
C 1s, C-F	-0.82 eV V^{-1}	0.14 eV V^{-1}	-0.89 eV V^{-1}
C 1s, C-C	-0.82 eV V^{-1}	0.15 eV V^{-1}	-0.88 eV V^{-1}
N 1s, N-C	-0.84 eV V^{-1}	0.13 eV V^{-1}	-0.63 eV V^{-1}
N 1s, N-S	-0.84 eV V^{-1}	0.12 eV V^{-1}	-0.58 eV V^{-1}
O 1s	-0.84 eV V^{-1}	0.09 eV V^{-1}	-0.38 eV V^{-1}
F 1s	-0.86 eV V^{-1}	0.13 eV V^{-1}	-0.35 eV V^{-1}
S 2p _{3/2}	-0.82 eV V^{-1}	0.12 eV V^{-1}	-0.32 eV V^{-1}

At very highly positive potentials ($8.5 \leq E \leq 11.0 \text{ V}$), the BE vs. E slopes were very variable for the elements analysed, ranging from $-0.3 \dots -0.4 \text{ eV V}^{-1}$ for O 1s, F 1s, and S 2p_{3/2}; to -0.6 eV V^{-1} for N 1s; and to -0.9 eV V^{-1} for C 1s (Table 1, Figure S1a–i). Thus, it seems that the oxygen, fluorine, and sulphur atoms were strongly (because of the partial-charge transfer (oxidation) step), nitrogen atoms were moderately, and carbon atoms were weakly attached to the aluminium-electrode surface within the potential range of $8.50 \leq E \leq 11.0 \text{ V}$. The very large variation in the $dBE dE^{-1}$ values observed for the elements studied could indicate the electrochemical decomposition of TFSI⁻ anion at very high anodic potentials and the electrochemical instability (i.e., electrochemical decomposition (oxidation)) of the SEI formed at less positive potentials. (This phenomenon will be discussed in more detail in the following section describing the results of the electrochemical-impedance spectroscopy measurements.) Extrapolating BE vs. E relationships measured within the potential range of 3.00 V to 4.50 V and 8.5 to 11.0 V into the potential range of $4.5 \text{ V} < E < 8.5 \text{ V}$, it seems that the two $dBE dE^{-1}$ lines crossed at ca. $E = 7.5 \text{ V}$ for F 1s and S 2p, at ca. 8 V for O 1s, at ca. 8.3 V for N 1s, and at ca. 8.7 V for C 1s (Figure S1a–i).

3.2. Information from CV Measurements

In order to investigate the electrochemical properties of the N4111(TFSI) | Al interface in detail, first the CV measurements were initiated. The CV scans were always started at $E = 0.00 \text{ V}$ and then swept up to a more positive (i.e., turn-over) desired potential; after that, the potential was returned to the initial value. Two consecutive scans were conducted at

every selected turn-over potential that was then increased stepwise. The data of the second scan were used in the data-analysis process and are discussed in the text and shown in the figures.

The CV measurement (Figure 2), performed in the potential range of 0.00 V to 1.00 V (and reverse) at the potential sweep rate of $v = 1.0 \text{ mV s}^{-1}$, showed two voltammetric waves at $E = 0.38 \text{ V}$ and $E = 0.65 \text{ V}$. Both waves slowly disappeared as the CV potential sweep ranges were expanded towards more positive values. A very slow increase in the anodic current at $E \geq 0.75 \text{ V}$ was also reported in the studies by Kityk et al. [31], who explained this as the temporal event of the electro-oxidation of Al located at the end of micropores located in the Al_2O_3 layer covering the Al electrode. When the CV sweep ranges were extended towards more positive potentials, the anodic currents recorded near the maximum potential applied were higher than measured in the previous CV at less positive potentials (Figure S2a,b). It should be mentioned that this anodic process was totally irreversible. Additionally, the electro-oxidation process currents, measured during the potential forward sweeps, were smaller than they were at the same potential in the previous CV performed in the narrower potential range. Thus, the increase in the anodic currents applying more positive turnover potentials and the anodic current-value reduction at the same potential in the following CVs indicates the thickening of the Al_2O_3 passivating layer because of the possible electrochemical decomposition of some trace water that still very likely remained in N4111(TFSI) after very careful pre-treatment. This Al_2O_3 passivating layer-thickening process has been observed and explained in detail previously [4–6,11–14,17,22,23,25,26]. It is interesting to note that the values of $dBE \text{ d}E^{-1}$ were in the range of $-0.82 \dots -0.85 \text{ eV V}^{-1}$ (Table 1), showing the almost non-specific adsorption (interaction) of N4111(TFSI) at the Al surface up to $E = 3.00 \text{ V}$.

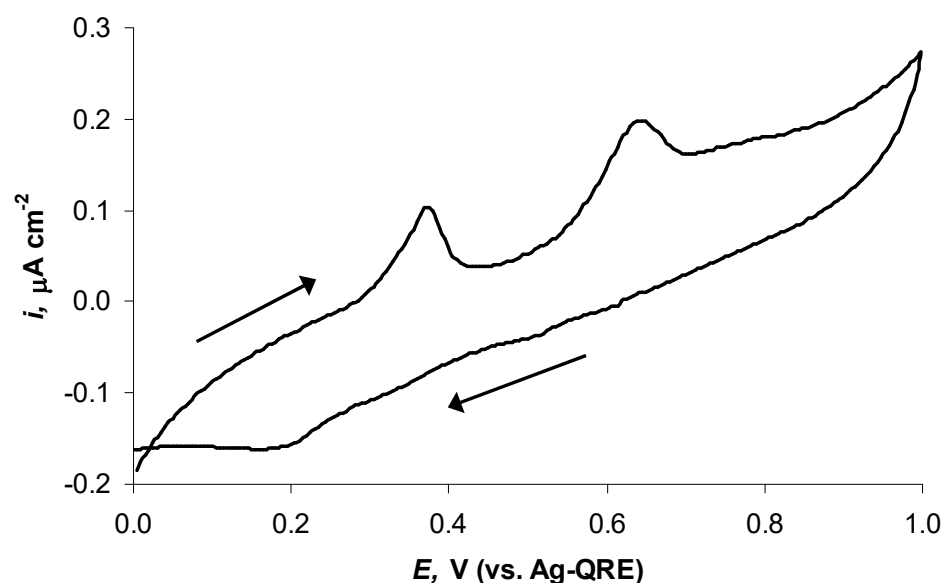


Figure 2. The cyclic voltammogram (CV) measured within the potential range of 0.00 V to 1.00 V and reverse at the potential sweep rate of 1.00 mV s^{-1} . The second CV sweep is presented; the potential sweep directions are indicated in the figures with arrows.

The electro-oxidation current measured voltammetrically began to increase intensively at $E = 2.75 \text{ V}$, when the CV potential sweep was conducted from 0.00 V to 3.00 V and reverse (Figures 3a and S2a–d). It is noteworthy that the $BE \text{ vs. } E$ dependence slope, calculated from in situ XPS $BE \text{ vs. } E$ data from 3.00 V to 4.50 V, increased to $0.10 \dots 0.15 \text{ eV V}^{-1}$, marking the chemisorption of N4111(TFSI) (Table 1). Thus, based upon the CV and in situ XPS data, we can conclude that at $E \geq 2.75 \text{ V}$ the irreversible electrochemical oxidation of Al started leading to the formation and deposition of N4111(TFSI)-insoluble $\text{Al}(\text{TFSI})_3$ onto the Al surface. Extending the CV sweep ranges toward more positive values than

$E = 3.5$ V, the Al/Al₂O₃ electrode became more activated step by step while the anodic currents had already started to increase at less positive potentials (Figure S2a–c). Thus, it seems that the Al-electrode-passivating Al₂O₃ layer decomposed and detached from the Al-electrode surface at $E \geq 3.0$ V and Al³⁺ cations formed at the Al surface reacted with (TFSI)[−] anions, leading to the specific adsorption of N4111(TFSI) at the Al electrode (Table 1). However, the formed Al(TFSI)₃ SEI could not prevent continuous Al-current-collector electro-oxidation [11,17,22,25,26,39].

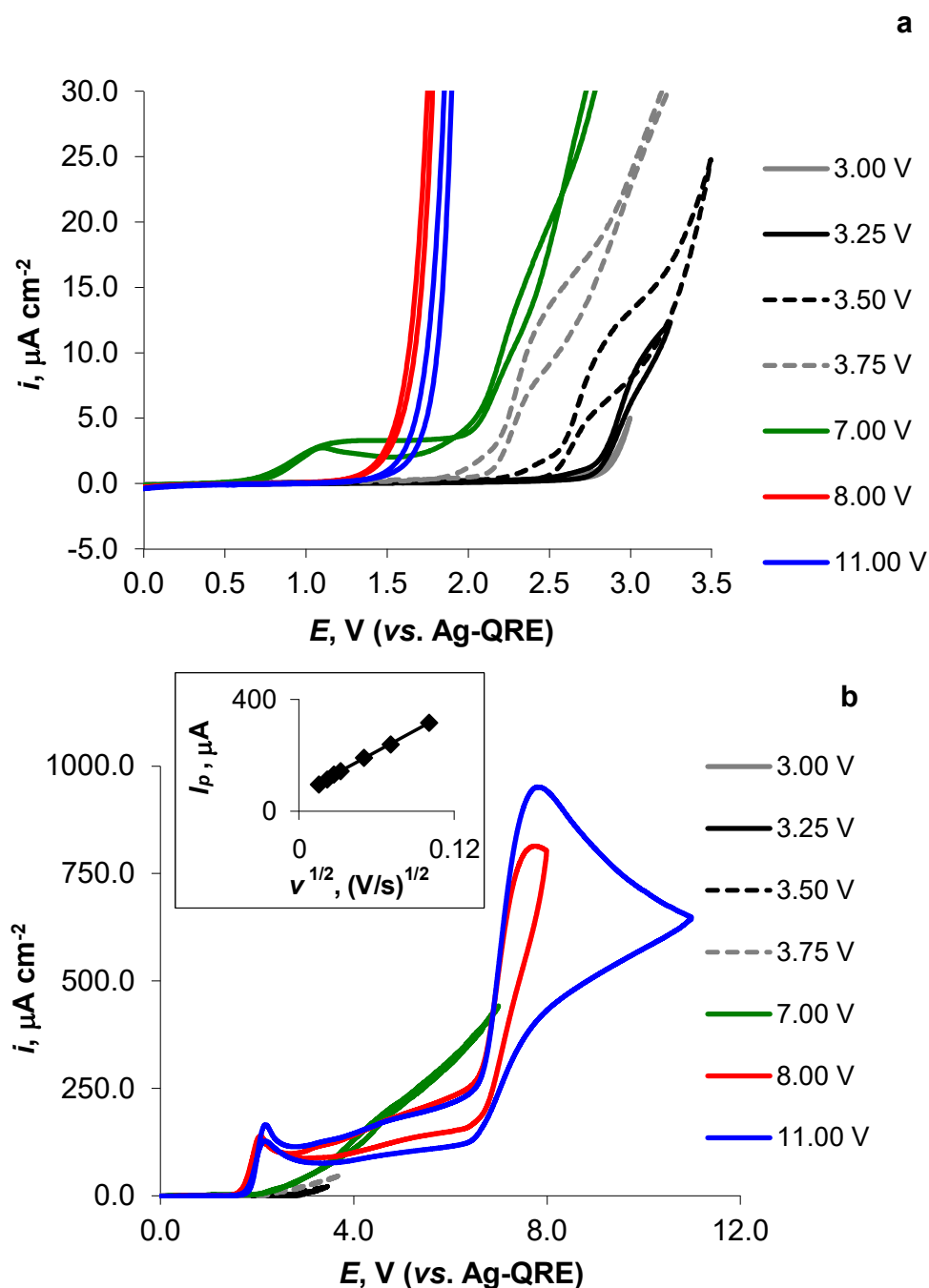


Figure 3. The cyclic voltammograms (CV), shown in different i and E scales, measured within the potential range from 0.00 V to the final potentials (indicated in the figure) and reverse at the potential sweep rate of 1.00 mV s^{-1} (a,b). The second CV sweeps are presented; the potential sweep directions are indicated in the figures with arrows. I_p vs. $v^{1/2}$ relationship, for the electro-oxidation process at $E = 7.8$ V, is shown in (b).

When the CV sweep was reversed at $E = 7.00$ V, an intensive electrochemical process started at $E = 0.65$ V, forming an anodic current peak at $E = 1.10$ V ($i = 2.7$ mA cm⁻²) (Figure 3a, green line, and Figure S3a–d). This electrochemical process can be connected with the intensive electro-oxidation of the Al₂O₃-film unprotected Al electrode and by the formation of Al(TFSI)₃, as described previously (Figures 2, 3a and S2a–c). It is important to note that when the Al electrode potential started to decrease during the CV reverse sweep, the current almost followed the path of the previous anodic (forward) sweep. After intensive electrochemical oxidation of Al at $E = 7.0$ V, changing the potential sweep direction towards the initial potential, $E = 0.0$ V, the current stood at a plateau from $E = 1.85$ V to $E = 1.20$ V. Thereafter, the anodic current decreased somewhat, forming an S-shaped voltammetric wave. No more electrochemical processes were observed in the potential range of $0.0 \text{ V} \leq E \leq 0.60 \text{ V}$, which indicates the electrochemical stability of Al in this potential range (Figures 3a, S2a–c and S3a–d). It should be noted that the shape of the measured CV curve (Figure 3a, green line) is very similar to the potential linear-sweep data presented by Kityk et al. [31] and measured during the Al-electropolishing process.

When performing the CV measurements within the potential range of 0.00 V to 8.00 V and 0.00 V to 11.0 V and reverse, a voltammetric peak formed in the forward and reverse scans at $E = 2.1$ V (Figures 2c,d and 3b). The anodic-current peak (I_p) values for the forward scan, measured at $E = 2.1$ V, were in a linear correlation with the v applied ($10 \text{ mV s}^{-1} < v < 50 \text{ mV s}^{-1}$, $R^2 = 1.00$). The shape of the measured CV curves near $E = 2$ V and the oxidation-current peak behaviour (e.g., the irreversibility of the electro-oxidation process) indicate the specific adsorption/desorption process of TFSI⁻ anions (as well as of N4111(TFSI), Table 1, Figure S1a–i) taking place at ca. $E = 2.1$ V at the previously activated Al electrode (Figures 3b and S2c,d). We believe that the electrochemical decomposition of N4111(TFSI) was unlikely near $E = 2$ V, as that process should have a diffusion speed-limited character, and we did not see visually or from the shape of the I vs. E relationships the formation of gas bubbles.

Continuing the potential forward scan, the oxidation current started to increase again at $E \geq 6.50$ V, leading to the formation of an anodic-current peak at ca. $E = 7.85$ V (Figures 3b and S2c,d). This oxidation-peak size increased when the CV forward-sweep range was extended to more positive values, indicating electrochemical activation of the Al electrode.

The analysis of the CV data, measured in the potential range of 0.0 V to 11.0 V and at various potential scan rates, indicated that the electro-oxidation process forming a current peak at $E = 7.80$ V ($v = 1.0 \text{ mV s}^{-1}$, $i = 0.91 \text{ mA cm}^{-2}$) was diffusion-speed limited, whereas the relationship between the oxidation I_p vs. $v^{1/2}$ was linear with a slope of $2.6 \times 10^{-3} \text{ A s}^{1/2} \text{ V}^{-1/2}$ ($0.25 \text{ mV s}^{-1} \leq v \leq 50 \text{ mV s}^{-1}$, $R^2 = 1.00$) (Figure 3b, inset). Thus, due to the very large intensity, irreversibility, and the shape of the CV curves near $E = 7.8$ V, we believe that this diffusion-speed-limited process is connected with the electro-oxidation of the TFSI⁻ anion itself. The electrochemical oxidation of the TFSI⁻ anion can also explain the large variations in the BE vs. E slope values for the 1 s in situ X-ray spectra of the elements studied (Table 1). However, although no changes are distinguishable in the shapes of the in situ X-ray spectra (measured in the potential range of $E = 0.0$ V to $E = 11.0$ V (Figure 1)), except for the reduction of the PE-signal intensity, the formed TFSI⁻ electro-oxidation products remained very likely at the N4111(TFSI) | Al/Al₂O₃ interface (i.e., under thick N4111(TFSI) layer) or evaporated into the vacuum.

Although no Al 2p XPS signal was observed in situ within the potential range applied and studied, it confirms the results of previous studies [4,23,40,41] that all Al³⁺ ions formed at the Al surface left near the N4111(TFSI) | Al/Al₂O₃ interface (i.e., that the salts of Al are insoluble in RTIL).

3.3. Results of Potentiostatic EIS Measurements

The potentiostatic EIS data were collected within the frequency range of 300 kHz down to 4 mHz, and a potential modulation amplitude of 5 mV was applied. The N4111(TFSI) | Al/Al₂O₃ system was given 120 s to relax at the selected potential before the start of the EIS measurement. The data of the second measurement were used for the following analysis. At the end of the second EIS measurement, the Al electrode potential was changed to a value 0.1 V higher. Using this method, the Al current collector was polarised and investigated in the range of 0.0 V to 8.0 V.

Nyquist plots, i.e., the relationships of the imaginary vs. real parts ($-Z''$ vs. Z') of the electrochemical impedance measured in the potentiostatic regime, are presented in Figure 4a–c. The $-Z''$ vs. Z' dependences are characteristic for mixed kinetic processes (adsorption and mass-transfer step limited) and showed high $-Z''$ values at very low frequencies within the potential range of 0.00 V to 0.50 V (Figure 4a), indicating the absence of faradic processes and marking that the Al surface covered with Al₂O₃ [11,17,22,25,26] behaved like an ideal capacitor. The Nyquist plot measured at $E = 0.70$ V had much lower Z' and $-Z''$ values at lower comparable frequencies and were moderately bent, indicating a finite length-diffusion process at Al/Al₂O₃ (i.e., some pitting corrosion) process at that potential (Figure 4a), notable also in the CVs (Figure 2). At $E \geq 0.80$ V, the size of $-Z''$ vs. Z' curves increased somewhat towards larger Z' and $-Z''$ values, indicating the filling of the pits and pores, leading to the decreasing of the pitting-corrosion speed at the Al electrode.

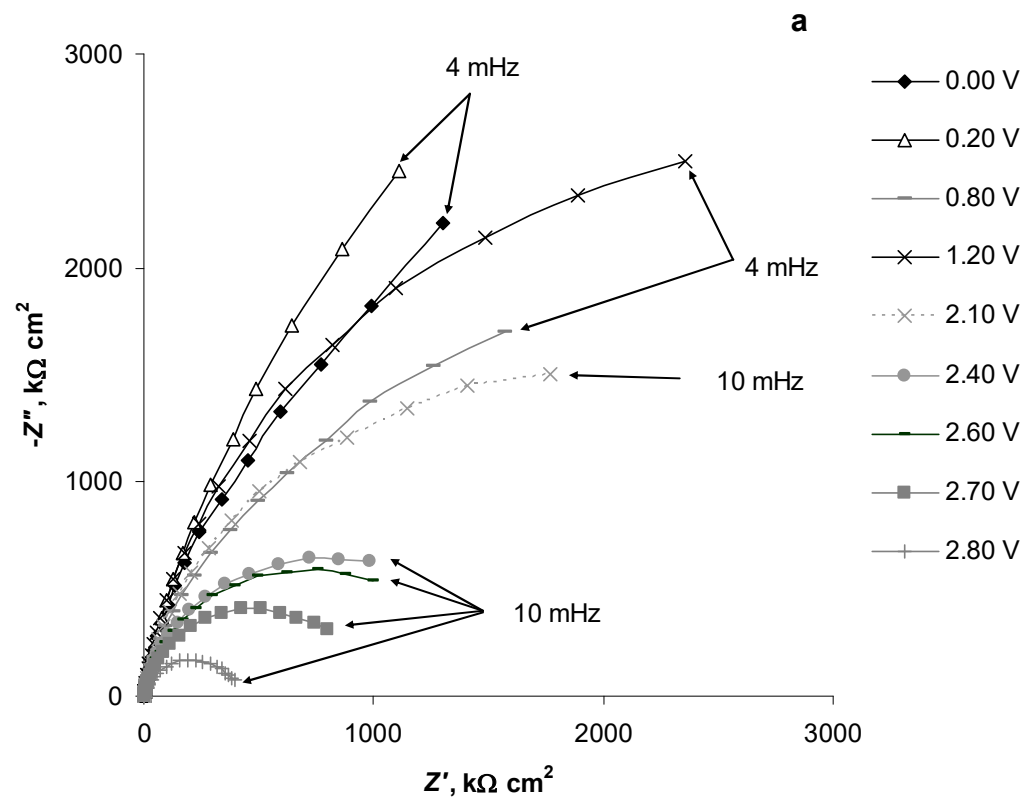


Figure 4. Cont.

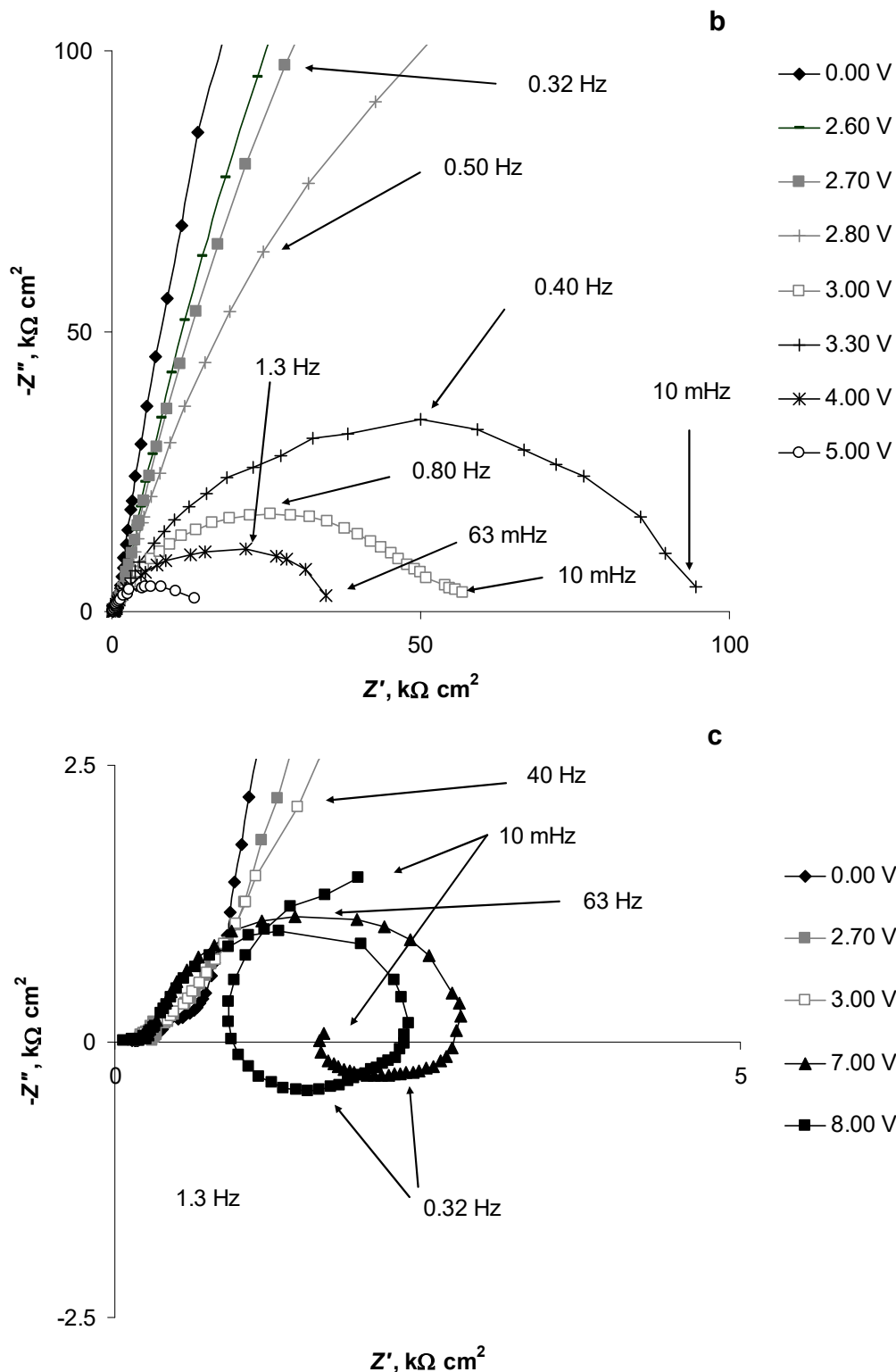


Figure 4. Nyquist plots, shown in various scales, for the N4111(TFSI) | Al/Al₂O₃ system measured at fixed potentials noted in the figures (a–c).

It is remarkable that the curves had the highest impedance values at the potentials 1.20 V and 1.30 V (higher than at $E = 0.70$ V or 0.80 V), marking intermediate passivity of the N4111(TFSI) | Al system. At more positive potentials than $E = 1.30$ V the Z' and $-Z''$ values started slowly to reduce, and at $E > 2.10$ V a steep activation of the N4111(TFSI) | Al

system took place due to the start of the electro-oxidation of Al (discussed previously and notable in Figure 3a), leading to a significant reduction of the appropriate impedance values and the formation of the semi arcs in the Nyquist-plot characteristic for diffusion and faradic step-limiting processes (Figure 4a). The measured impedances were similar within the potential range from 2.40 V to 2.60 V, forming a group of semicircles. A current plateau was also notable in Figure 4 at $2.30 \text{ V} < E < 2.60 \text{ V}$. At $E \geq 2.70 \text{ V}$; the activity of the N4111(TFSI) | Al system started to increase further (Figure 4a). A tiny semicircle formed in the Nyquist plot at $E = 3.00 \text{ V}$, indicating the intensification of the electrochemical processes at the N4111(TFSI) | Al/Al₂O₃ interface (Figure 4b). This corresponds to the potential when the N4111(TFSI) started to chemisorb as the BE vs. E slopes became close to unity for the studied elements (Figure 3a and Table 1). The semicircle size (i.e., the maximum values of Z' and $-Z''$) increased thereafter for a moment and continued to decrease again at $E > 3.30 \text{ V}$ (Figure 4b). (It is possible that this temporal reduction in the Al oxidation speed was caused by partial blocking of the Al/Al₂O₃ surface by adsorbed N4111(TFSI) and formed Al(TFSI)₃.) The following reduction of the Z' and $-Z''$ values parallel with the increase of the Al electrode potential indicates the intensification of the Al electro-oxidation process. At $E = 7.00 \text{ V}$ and 8.00 V (Figure 4c), inductive loops formed in the low-frequency part of the EIS spectrum, indicating intense electrochemical oxidation and dissolution of the Al electrode, leading to probable roughening and expansion of its surface (Figure 4c), which is also visible as the high-intensity electro-oxidation current peak in the CV curve at $E = 7.90 \text{ V}$ in Figure 3b. This means that at ca. $E = 7.0 \text{ V}$, when the TFSI⁻ anions electro-oxidation started (discussed previously), Al started to dissolve non-uniformly and the surface became rough. It is likely that the intense Al surface (e.g., expansion of the Al surface area) or near the Al surface-related relaxation processes, initiated by the intensive electrochemical oxidation of TFSI⁻ anions, are responsible for the formation of the inductive loops in the low-frequency part of the EIS Nyquist plot (Figure 4c) [13,42]. Due to the high physical instability of the N4111(TFSI) | Al/Al₂O₃ system, the measured EIS data were noisy at the potentials higher than 8.00 V, and therefore, at more positive potentials collected EIS data analysis was impossible.

Figure 5a shows that the $\log |Z''|$ vs. \log -frequency (ν) plots were linear with a slope of -0.84 in the $\log \nu$ range from -1.60 (Hz) to 3.80 (Hz) and in the potential range of 0.00 V to 2.10 V , indicating that the N4111(TFSI) | Al/Al₂O₃ system behaved almost like an ideally polarisable system. At $E \geq 2.40 \text{ V}$, a maximum started to form at low frequencies. By increasing the Al/Al₂O₃ electrode potential, this $\log |Z''|$ maximum moved towards higher frequencies and obtained a peak-like shape. This change in the $\log |Z''|$ vs. $\log \nu$ plot shapes indicated the activation of the Al/Al₂O₃ electrode and the start of faradic processes. The $\log |Z''|$ vs. $\log \nu$ plots, measured at $E = 7.00 \text{ V}$ and $E = 8.00 \text{ V}$, had two characteristic minimums at $\nu = 3.9 \text{ Hz}$ and $\nu = 16 \text{ mHz}$, and at $\nu = 7.9 \text{ Hz}$ and $\nu = 63.2 \text{ mHz}$ (corresponding to $|Z''| = 0$ in the Nyquist plots), respectively (Figure 5a).

$\log |Z|$ vs. $\log \nu$ plots were linear in the $\log \nu$ range from -2.40 to 1.60 (Hz) and in the potential range from 0.00 V to 2.40 V with a slope of -0.88 (Figure 5b). However, at $E \geq 2.40 \text{ V}$ it started to bend, and at the lowest frequencies it formed a plateau, indicating that the N4111(TFSI) | Al/Al₂O₃ system entered the mixed kinetic region. As the Al-electrode potential increased, the plateau started to form at higher frequencies and had a lower $\log |Z|$ value. The $\log |Z|$ vs. $\log \nu$ plot, measured at $E = 7.0 \text{ V}$, had a $\log |Z|$ plateau that started to form at $\log \nu \leq 1.60$ (Hz), obtaining a $\log |Z|$ maximum at $\log \nu = 0.95$ (Hz), and then started to continuously decrease with a very small slope at lower frequencies (Figure 5b). The $\log |Z|$ vs. $\log \nu$ plot, measured at $E = 8.0 \text{ V}$, also started to form a $\log |Z|$ plateau at $E \leq 1.60$ (Hz); however, since it passed a $\log |Z|$ maximum at $\log \nu = 1.09$ (Hz), the values of $\log |Z|$ started very slowly to reduce again. At $\log \nu = -0.6$ (Hz) the reduction intensified and formed a minimum ($\log |Z| = 2.97$) at $\log \nu = -1.30$ (Hz) (Figure 5b). The minimum formed at the $E = 8.0 \text{ V}$ measured $\log |Z|$ vs. $\log \nu$ plot's low-frequency section overlapped with the low-frequency inductive loop and

the start of a new semi-circle (visible in the Nyquist plot, Figure 4c), indicating the presence of a slow reorganisation process at the N4111(TFSI) | Al interface.

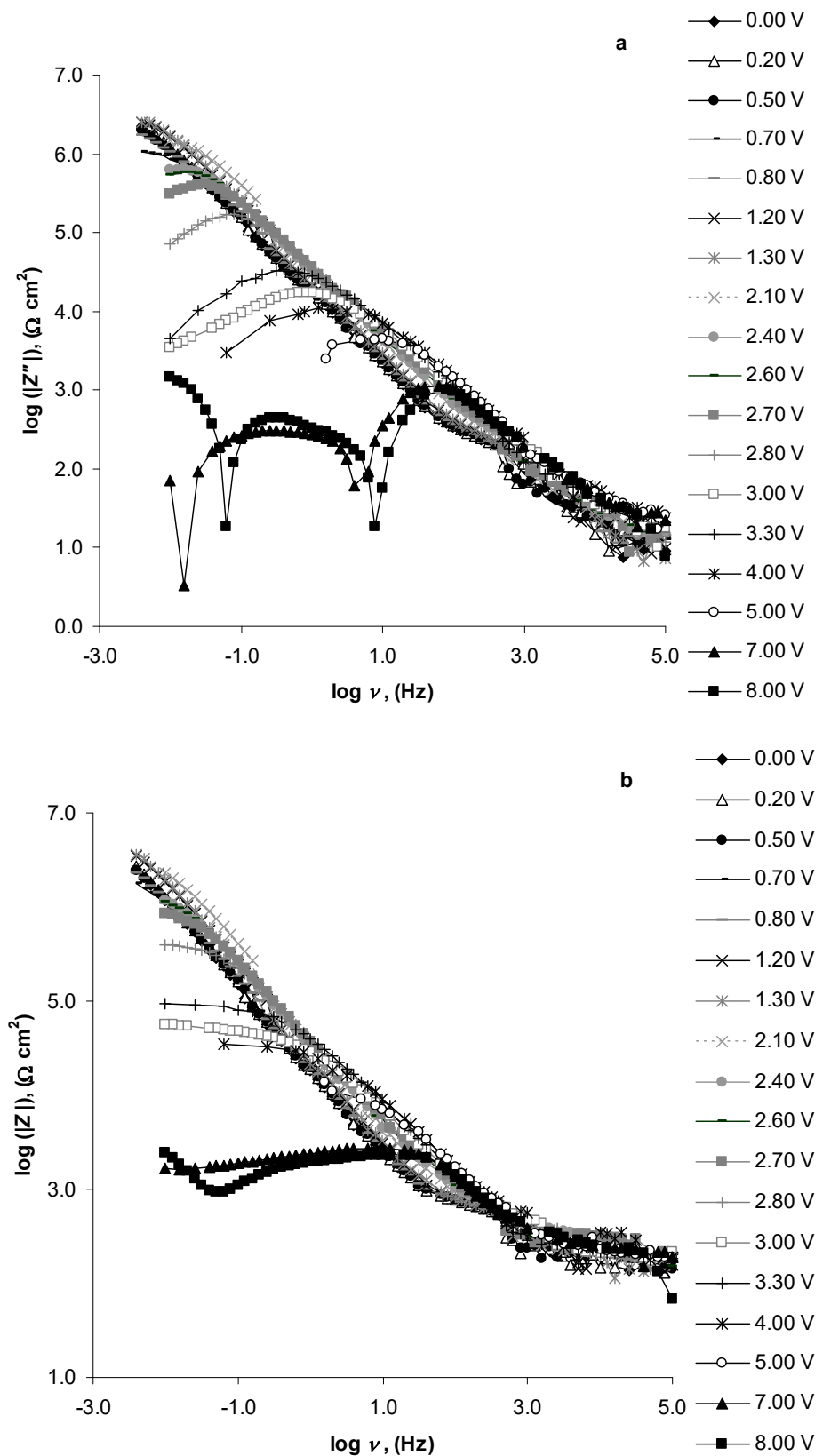


Figure 5. Cont.

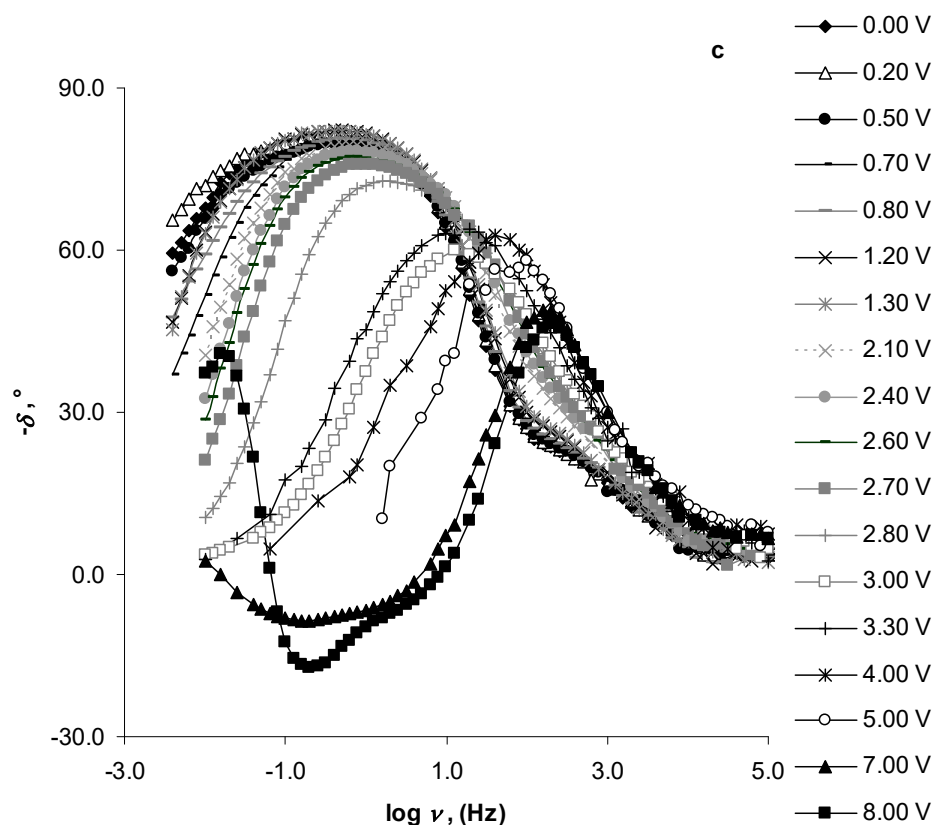


Figure 5. Bode plots for the N4111(TFSI) | Al/Al₂O₃ system measured at fixed Al-electrode potentials noted in the figures: $\log |Z''|$ vs. $\log \nu$ (a); $\log |Z|$ vs. $\log \nu$ (b), and $-\delta$ vs. $\log \nu$ (c).

The phase angle (δ) vs. $\log \nu$ plots (Figure 5c) show that the N4111(TFSI) | Al/Al₂O₃ system was nearly ideally polarisable at $E = 1.20$ V and $E = 1.30$ V, when the phase angles were the most negative $\delta = -82^\circ$ ($\nu = 0.40$ Hz), as noted in the Nyquist plots at the same potentials (Figure 4a). At more positive Al potentials, the phase-angle values started slowly to increase. That process intensified at $E > 2.60$ V, marking the start of faradic processes. It is remarkable that the second phase-angle peak formed in the $-\delta$ vs. $\log \nu$ plot at $E = 8.00$ V and $\log \nu = -1.80$ (Hz) (Figure 5c). This phase-angle peak indicates the presence of the second adsorption-step limited electrochemical process, having a much smaller time constant and running parallel to the Al electro-oxidation process.

The series-capacitance (C_s) values, measured at the EIS modulation frequency $\nu = 0.10$ Hz and calculated as described in Refs. [43,44], were very stable until $E = 3.00$ V, when a capacitance peak formed ($C_s = 0.17$ mF cm⁻²), indicating a strong (specific) adsorption or faradic process at the Al electrode. The second C_s increase was at $E = 3.60$ V (Figure 6), indicating the expansion of the SEI layer. This information is in good agreement with the in situ XPS and CV data discussed previously and confirms N4111(TFSI)-specific adsorption with a partial charge-transfer step at the Al/Al₂O₃ electrode, followed by Al(TFSI)₃ formation at the electrode surface.

It should be mentioned that it was impossible to analyse EIS data, collected at $\nu = 0.10$ Hz, for the N4111(TFSI) | Al system within the potential range of 3.60 V $< E < 7.00$ V while the recorded spectrum was unstable at low modulation frequencies. This instability was caused by intensive electro-oxidation of the Al electrode, adsorption of N4111(TFSI) at the Al/Al₂O₃ interface, and the formation of Al(TFSI)₃. The C_s values at $E = 7.00$ V and $\nu = 0.10$ Hz ($C_s = -6.1$ mF cm⁻²) and $E = 8.00$ V and $\nu = 0.10$ Hz ($C_s = -6.8$ mF cm⁻²) were negative due to the formation of the inductive loops in the EIS spectra caused by intensive electrochemical oxidation of the TFSI⁻ anion, dissolution of the Al electrode, and reorganisation of the Al surface at these potentials (Figures 4c, 5a–c and 6) [13,42].

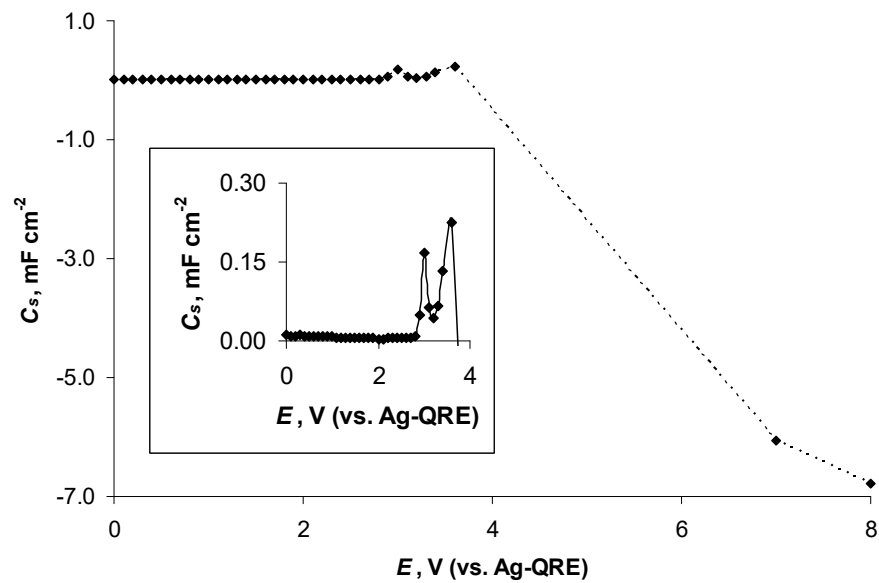


Figure 6. Series capacitance (C_s) vs. Al-electrode-potential (E) relationship at the electrochemical-impedance-spectroscopy modulation frequency of 0.10 Hz.

The parallel-capacitance (C_p) values (describing the capacitance of the electrical double layer at the electrode surface), measured at the modulation frequency $\nu = 0.10$ Hz and calculated from the impedance data [44], showed a similar trend, presented in Figure 6, for C_s . Values of C_p slightly decreased from 0.00 V to 3.60 V, indicating that the properties of the electrical double layer changed very little at N4111(TFSI) | Al/Al₂O₃ in this potential region (Figure 7). At $E > 3.60$ V, the N4111(TFSI) | Al system became unstable. However, the C_p values, calculated from the EIS low-frequency data measured at $E = 7.00$ V and $E = 8.00$ V, were significantly reduced. The negative values of $C_p = -0.12$ mF cm⁻² at $E = 7.00$ V and -0.37 mF cm⁻² at $E = 8.00$ V were caused by intensive electrochemical oxidation processes, leading to the formation of the inductive loop in the EIS Nyquist plot at the low-frequency section. Thus, the intensive electro-oxidation and dissolution of the Al electrode, electro-oxidation of the TFSI⁻ anion, and variable relaxation processes, including the instability of the electrical double layer, took place at the N4111(TFSI) | Al interface [13,42].

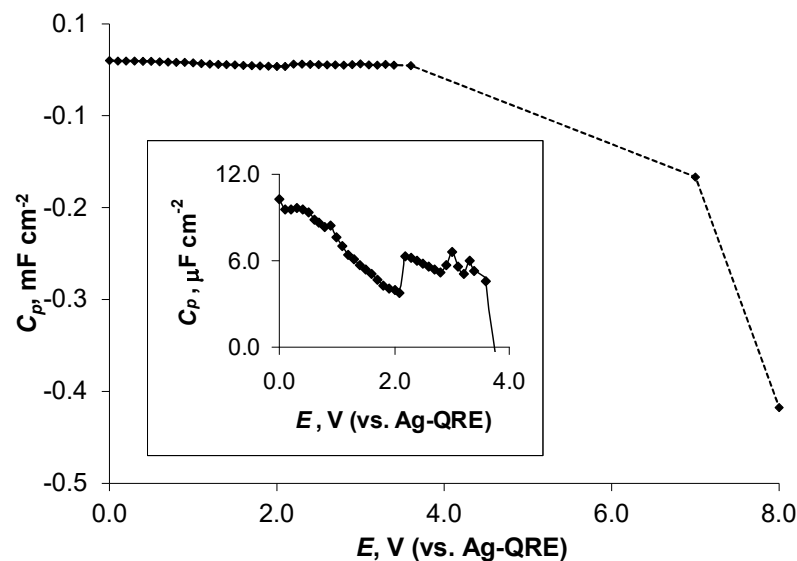


Figure 7. Parallel capacitance (C_p) vs. Al-electrode-potential (E) relationship at the electrochemical-impedance-spectroscopy modulation frequency 0.10 Hz.

The dependence of the ratio $C_p \cdot C_s^{-1}$ on E , being an indicator of the ideal polarisability of an investigated electrochemical system [44], had the closest values to the unity from $E = 0.00$ V to $E = 2.60$ V (from $C_p \cdot C_s^{-1} = 0.97$ to 0.88 , respectively) (Figure 8). The N4111(TFSI) | Al system was nearly ideally polarisable up to $E = 2.60$ V ($C_p \cdot C_s^{-1} = 0.88$), marking the end of the high-stability region for the N4111(TFSI) | Al interface. At more positive potentials, a steep decrease in the $C_p \cdot C_s^{-1}$ values took place, obtaining a minimum at $E = 3.00$ V ($C_p \cdot C_s^{-1} = 0.04$) corresponding to a high-intensity charge-transfer process due to the start of intensive electrochemical oxidation of the Al electrode (Figures 3a and 8).

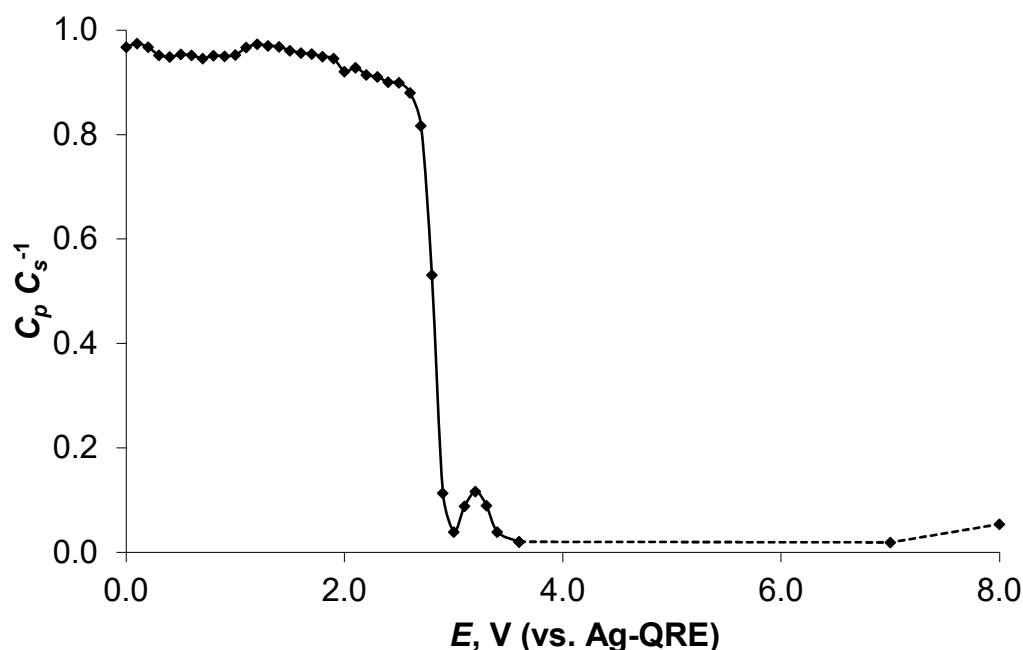


Figure 8. The ratio of parallel (C_p) and series (C_s) capacitance ($C_p C_s^{-1}$) vs. Al-electrode potential (E), applied; relationship at the electrochemical-impedance-spectroscopy modulation frequency of 0.10 Hz.

The values of imaginary capacitance C'' , measured at the modulation frequency $\nu = 0.10$ Hz, were calculated as in refs. [44,45]. High C'' values indicate the presence of energy dissipation by an irreversible electro-oxidation process that leads to the appearance of hysteresis (e.g., to the formation of the current hysteresis in the CV curves (Figures 3a, S2a–d and S3a–d) or to the formation of the inductive loops in the Nyquist plots at very low ν values (Figure 4c)) [45]. The C'' vs. E graph showed a peak at $E = 3.00$ V ($C'' = 33 \mu\text{F cm}^{-2}$), i.e., at the potential of starting the specific adsorption of N4111(TFSI) and electro-oxidation processes at Al (i.e., the formation of $\text{Al}(\text{TFSI})_3$) according to the in situ XPS measurements (Table 1), followed by a continuous increase in the values of C'' at $E > 3.20$ V up to $C'' = 1.4 \text{ mF cm}^{-2}$ at $E = 8.00$ V (Figure 9) when the low-frequency inductive loop appeared in the Nyquist plot (Figure 4c). It must also be mentioned that at $3.00 \text{ V} < E < 6.50 \text{ V}$, intensive Al electro-oxidation and the formation of N4111(TFSI)-insoluble $\text{Al}(\text{TFSI})_3$ was observed. Thus, the C'' data are in very good agreement with the in situ XPS and voltammetric-measurement results.

It should be noted that the series resistance (R_s), calculated from the EIS fitting data and describing the electrode material (i.e., current collector) + SEI + electrolyte resistance, was stable ($R_s = 250 \pm 50 \Omega \text{ cm}^2$) throughout the potential range applied ($0.00 \text{ V} \leq E \leq 8.00 \text{ V}$) (Figure 10a). This indicates that the electrolyte resistance gave the largest contribution to the R_s value. The high values of parallel resistance (R_p), calculated from the EIS fitting data and reflecting the low intensity of faradic processes or the slow mass-transport step of ions through the SEI layer, were reduced with the application of more positive potentials passing an intermediate minimum at $E = 0.70$ V ($R_p = 2.5 \text{ M}\Omega \text{ cm}^2$) and a maximum at

$E = 1.30 \text{ V}$ ($R_p = 6.2 \text{ M}\Omega \text{ cm}^2$), decreasing continuously thereafter due to the intensification of the faradic processes (Figure 10a).

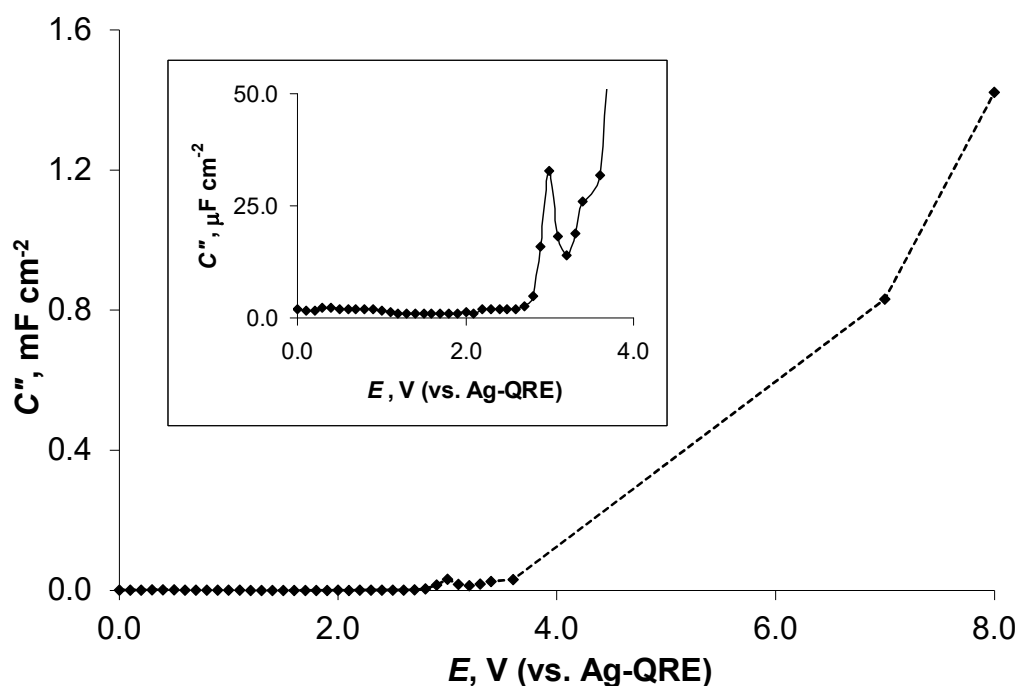


Figure 9. Imaginary capacitance (C'') vs. potential (E) applied to the Al current collector. C'' values were calculated using impedance-spectroscopy data measured at the modulation frequency of 0.1 Hz.

C_s , C_p , $C_p C_s^{-1}$, R_s , and R_p data reflect the complicated and sophisticated nature of the N4111(TFSI) | Al/Al₂O₃ system and the SEI-formation process at the Al/Al₂O₃ surface in N4111(TFSI). The EIS data indicate that Al current collectors, covered initially only with a thin layer of Al₂O₃ and formed in dry air at room temperature, can be polarised in N4111(TFSI) (as the electrolyte in the EDLC) up to $E = 2.6 \text{ V}$. At more anodic potentials, intensive faradic processes started to be reflected by the steep reduction of the $C_p C_s^{-1}$ ratio. We propose that at $E > 2.6 \text{ V}$, intensive electro-oxidation process of the Al-current-collector interface started leading to the formation of an Al(TFSI)₃ (and probably also AlF₃) layer at $E \geq 3.00 \text{ V}$.

It should be mentioned that the R_s and R_p values at $E = 7.00 \text{ V}$ and $E = 8.00 \text{ V}$, respectively, were calculated from the EIS data based on the simple equivalent circuit shown in Scheme 1. However, it is obvious from the Nyquist and Bode plots that this simple circuit did not describe the real situation, i.e., the formation of the low-frequency inductive loops at $E = 7.00 \text{ V}$ and $E = 8.00 \text{ V}$, respectively. Therefore, the EIS data at $E = 7.00 \text{ V}$ should be fitted using the equivalent circuit shown in Scheme 2a, which is very similar to the one described in [13,46–48]. This equivalent circuit contains (1) a resistor in series (R_s), (2) a first oscillation ring containing a resistor (R_1) and a constant phase element (CPE_1) connected in parallel, and (3) a second oscillation ring containing a resistor (R_2 marking charge-transfer resistance), a constant phase element (CPE_2), and an inductor (describing the expansion of the electrochemically active surface area of the Al electrode, i.e., the increase in the surface roughness) connected in parallel. The first (i.e., high-frequency) oscillation ring describes the restricted mass transport through the porous SEI formed at the Al electrode. The second (i.e., mid-frequency) oscillation ring describes the irreversible electro-oxidation of the Al electrode and the expansion of the Al-electrode area (i.e., the roughening of the Al-electrode surface). In the fitting process obtained, the Nyquist plot is shown (see Figure S4). The equivalent circuit elements had the following values: $R_s = 0.22 \text{ k}\Omega \text{ cm}^2$, $R_1 = 1.7 \text{ k}\Omega \text{ cm}^2$, $\text{CPE}_1 = 950 \text{ nF cm}^{-2}$, $R_2 = 0.89 \text{ k}\Omega \text{ cm}^2$, $\text{CPE}_2 = 26 \mu\text{F cm}^{-2}$ ($a = 0.85$), and $L = 1.1 \text{ kH}$. Although the Kramers–Kronig test yielded the result $X^2(Z) = 7.0 \cdot 10^{-12}$, we consider that

the recorded EIS data and the numerical values of the circuit elements calculated in the fitting process are trustworthy.

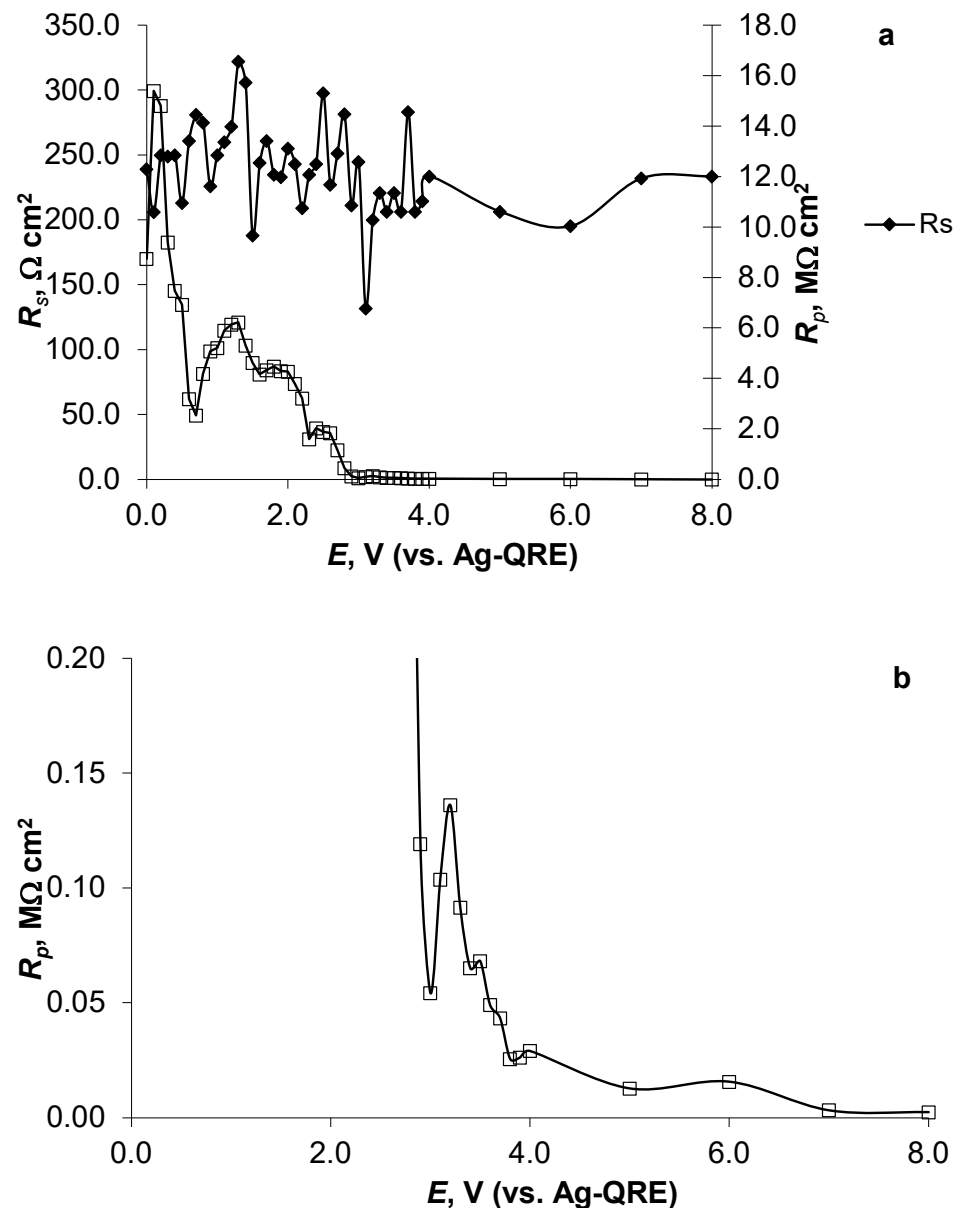
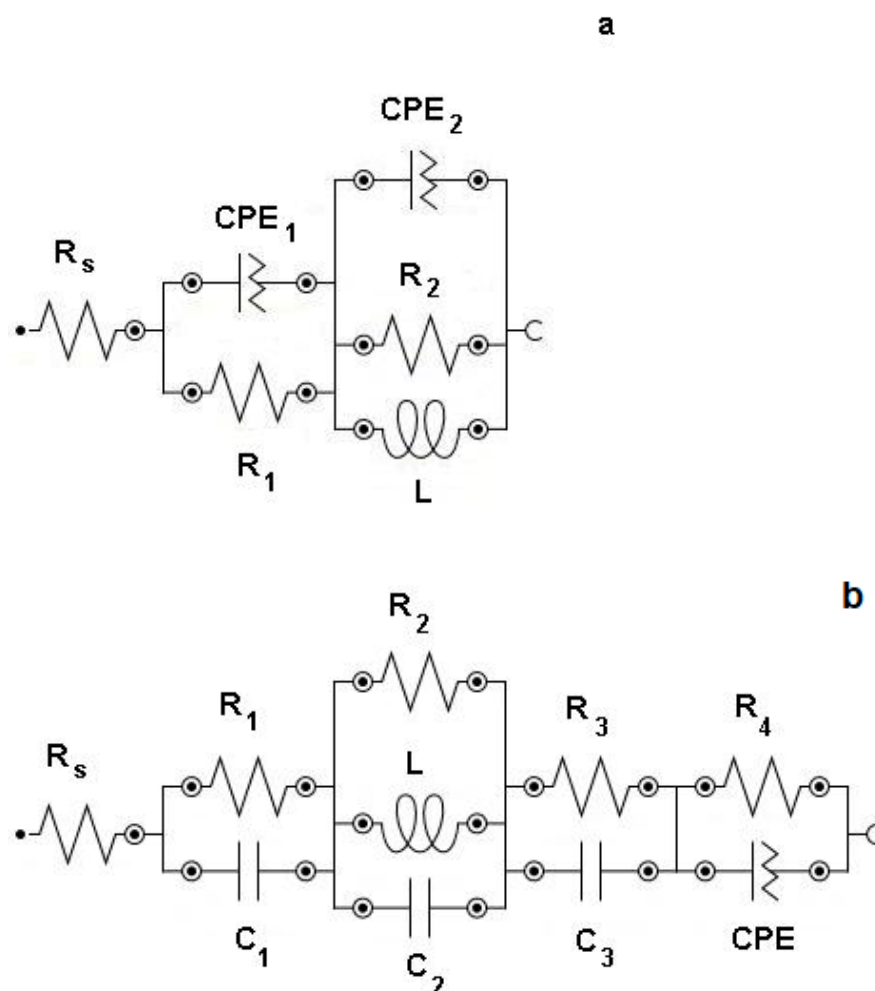


Figure 10. The series-resistivity (R_s) (a) and parallel-resistivity (R_p) (b) relationships vs. Al-electrode potential (E) applied.

The constructed equivalent circuit for the fitting of the EIS data measured at $E = 8.00 \text{ V}$ is based on the model used to describe the delayed breakdown and re-formation processes of the passive layer (SEI) taking place at oxidation (corrosion) Al [48]. The completed equivalent circuit is shown in Scheme 2b and is similar to the one described previously in Scheme 2a; however, some CPEs were replaced with real capacitors and one additional RC and R-CPE low-frequency oscillation ring was added. The third oscillation ring (R_4 and CPE) describes a process that has a very long time-constant value. The Kramers–Kronig test yielded for this equivalent circuit the result $X^2(Z) = 9.4 \cdot 10^{-6}$, and therefore we consider that the linearity condition was preserved at such a high anodic potential and intensive charge-transfer speed. The equivalent circuit elements had the following values: $R_s = 0.20 \text{ k}\Omega \text{ cm}^2$, $R_1 = 0.76 \text{ k}\Omega \text{ cm}^2$, $C_1 = 2.5 \mu\text{F cm}^{-2}$, $R_2 = 1.1 \text{ k}\Omega \text{ cm}^2$, $C_2 = 1.8 \mu\text{F cm}^{-2}$, $L = 1.1 \text{ kH}$, $R_3 = 5.4 \text{ k}\Omega \text{ cm}^2$, $C_3 = 9.3 \text{ mF cm}^{-2}$, $R_4 = 0.19 \text{ k}\Omega \text{ cm}^2$, and $\text{CPE} = 5.2 \text{ mF cm}^{-2}$.

($a = 0.72$). R_2 has also been defined in the literature [48] as the charge-transfer resistance. It should be noted that large inductance was found during the EIS data-modelling process, obtained at $E = 7.00$ V and $E = 8.00$ V. It is obvious that intensive electro-oxidation of the Al electrode, the adsorption of ions at the N4111(TFSI) | Al interface, and the reorganisation of the SEI reduced the quality of the measured EIS data at $E > 4.0$ V.



Scheme 2. The equivalent circuit to describe the N4111(TFSI) | Al/Al₂O₃ system at $E = 7.00$ V (a) and at $E = 8.00$ V (b).

The normalised active power $P(w)/S(w)$ (marked by the consumer-consumed charge (e.g., a faradic reaction) or electric power) and normalised reactive power $Q(w)/S(w)$ (marked by the energy-source reflected power, the so-called capacitive power) values were calculated as in [10,43–45,49–52] and their dependences upon the $\log \nu$ are shown for selected potentials in Figure S6. It is remarkable that the crossing of the $P(w)/S(w)$ vs. $\log \nu$ and $Q(w)/S(w)$ vs. $\log \nu$ lines took place at $P(w)/S(w) = Q(w)/S(w) = 0.70$ instead of at 0.50, which was observed for electrical double-layer capacitors with a reversible charging–discharging mechanism [10,43–45]. It should be noted that the crossing of the normalised power lines at $P(w)/S(w) = Q(w)/S(w) = 0.70$ was also observed in the literature [49–52]. $P(w)/S(w)$ vs. $\log \nu$ and $Q(w)/S(w)$ vs. $\log \nu$ lines crossed twice, indicating the existence of processes with two relaxation time constants [10,43–45,49–52] for the N4111(TFSI) | Al/Al₂O₃ system at all potential applied. These relaxation time constants can be estimated graphically as the frequency of the normalised power-line crossings (Figure S6). It is characteristic that the value of both the mid-frequency relaxation time constant $t(\text{rel}, 1)$ (Figure 11a) and the low-frequency relaxation time constant $t(\text{rel}, 2)$ (Figure 11b) increased as the Al-electrode potential increased. However, their

different dependences upon the potential applied to the Al electrode indicates the varied and sophisticated nature of these processes. The $t(\text{rel}, 1)$ decreased monotonously with the application of more positive potentials from $t(\text{rel}, 1) = 0.036$ s at $E = 0.00$ V to $t(\text{rel}, 1) = 0.0032$ s at $E = 3.70$ V linearly (slope = -0.01 s V^{-1} , $R^2 = 0.99$). At $E > 3.70$ V, it obtained an almost stable value: $t(\text{rel}, 1) = 0.003 \dots 0.004$ s until the highest potential applied to the Al electrode, i.e., $t(\text{rel}, 1) = 0.0036$ s at $E = 8.00$ V (Figure 11a). It should be mentioned that at $E > 3.60$ V the EIS spectrum measured became extremely unstable due to specific adsorption of N4111(TFSI) at the Al surface (Table 1) and intensive electro-oxidation of Al (probably leading to the roughening and expansion of the Al electrode surface) and the deposition of the Al-oxidation products (e.g., $\text{Al}(\text{TFSI})_3$) forming a porous and expanding SEI layer at the N4111(TFSI) | Al interface (Figures 3–10).

The values of $t(\text{rel}, 2)$, estimated graphically from $P(w)/S(w)$ vs. $\log \nu$ and $Q(w)/S(w)$ vs. $\log \nu$ plots measured at low potentials applied, were unstable, probably because of difficulties in their precise estimation from the graphs at $E \leq 0.60$ V. However, the estimated values of $t(\text{rel}, 2)$ seemed to increase from the initial value ($t(\text{rel}, 2) = 1200$ s, $E = 0.00$ V), as the Al/ Al_2O_3 electrode potential was changed stepwise to be more positive, forming a maximum $t(\text{rel}, 2) = 4000$ s at $E = 0.30$ V (Figure 11b). Thereafter, a steep reduction in $\log [t(\text{rel}, 2)]$ values was observed, showing a minimum at $E = 0.60$ V and $E = 0.70$ V. At more positive potentials than $E > 0.90$ V ($t(\text{rel}, 2) = 420$ s), a monotonous reduction in $\log [t(\text{rel}, 2)]$ values continued until a steeper decrease occurred at $E \geq 2.7$ V (Figure 11b). This remarkable change in $t(\text{rel}, 2)$ values overlapped with the activation of the Al electrode (steep reduction in the C_p , C_s^{-1} values, Figure 8). At $E > 2.90$ V (when a C_s peak formed at $E = 3.00$ V, Figure 6), a slow continuous decrease in the $t(\text{rel}, 2)$ values to $t(\text{rel}, 2) = 0.0067$ s was notable until the final potential of $E = 8.00$ V was applied (Figure 11b). Thus, the values of $t(\text{rel}, 2)$ reflect the electrochemical activity of the N4111(TFSI) | Al interface.

The approximation of $t(\text{rel}, 1)$ and $t(\text{rel}, 2)$ values, parallel to the increase in the Al electrode potential, is notable in Figure S6 as the formation of the overlapping $P(w)/S(w)$ vs. $\log \nu$ and $Q(w)/S(w)$ vs. $\log \nu$ line peaks after $E \geq 3.00$ V. For the $P(w)/S(w)$ vs. $\log \nu$ and $Q(w)/S(w)$ vs. $\log \nu$ relationships, measured at $E = 7.00$ V and $E = 8.00$ V, the presence of small “peaks” at $\log \nu = -0.70$ (Hz) is characteristic (Figure S6). Their formation indicates the start of new electrochemical processes running in parallel. These new processes could involve the relaxation (e.g., slow adsorption–desorption) processes at the N4111(TFSI) | Al interface, yielding a new low-frequency arc in the Nyquist plot measured at $E = 8.00$ V (Figures 4c and S5).

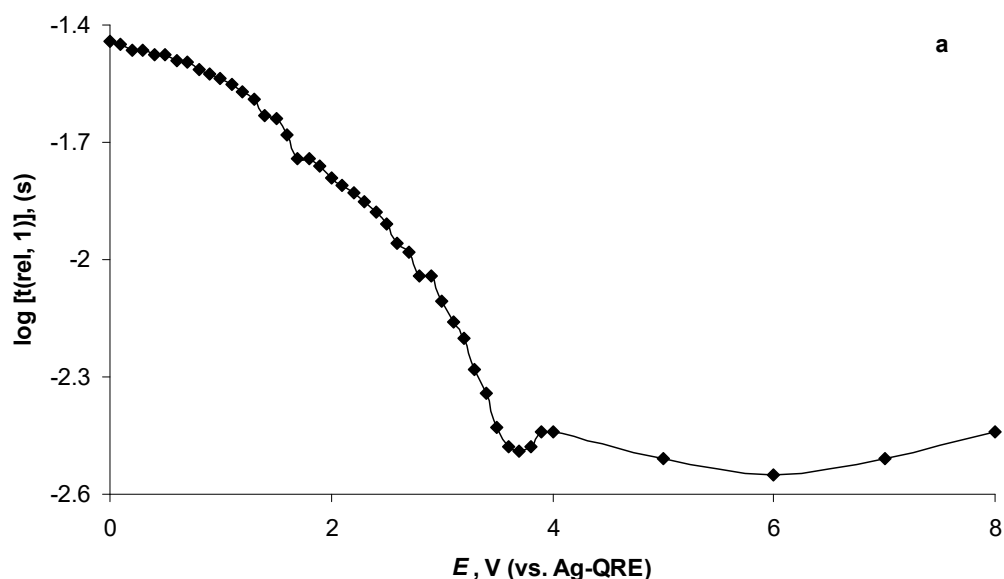


Figure 11. Cont.

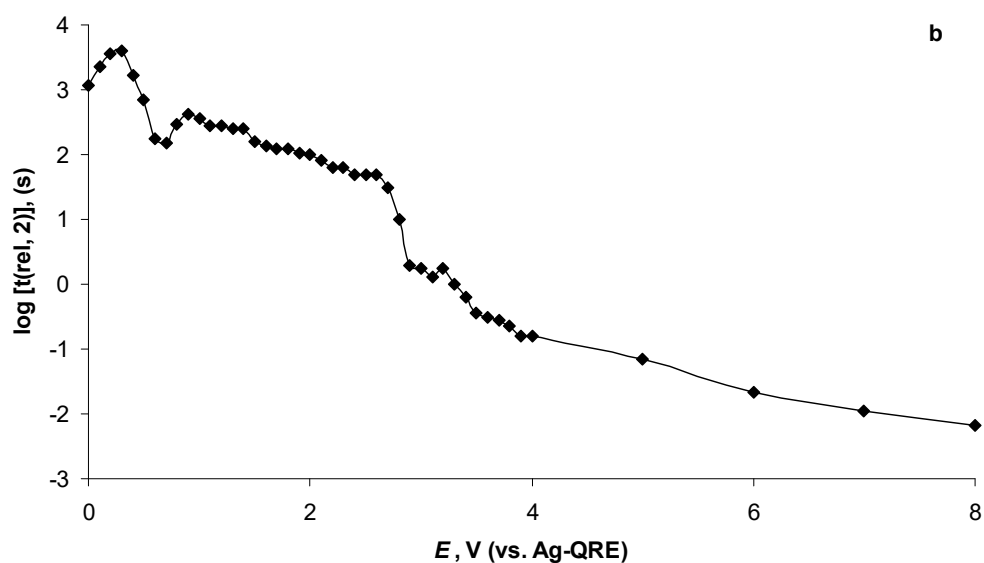


Figure 11. Mid-frequency relaxation time constant ($\log [t(\text{rel}, 1)]$) vs. E (a) and low-frequency relaxation time constant ($\log [t(\text{rel}, 2)]$) vs. E relationships (b).

4. Conclusions

The in situ soft X-ray photoelectron spectroscopy (XPS) data, measured for the first time in parallel with the cyclic-voltammetry (CV) and electrochemical-impedance-spectroscopy (EIS) investigations, yielded interesting new information about the electrochemical behaviour of the butyltrimethylammonium bis(trifluoromethylsulfonyl)imide [N4111(TFSI)] and Al/Al₂O₃ interface and Al-current-collector corrosion at high anodic potentials. CV, EIS, and in situ XPS data obtained in this study indicate that at $E \geq 2.6$ V (vs. Ag-QRE), intensive Al-electrode oxidation started. With the elements investigated in the in situ XPS method forming N4111(TFSI), inner-core electron-binding energy vs. applied-potential (BE vs. E) data show that at $E \leq 2.6$ V no intensive faradic oxidation processes occurred but at $E \geq 3.00$ V (vs. Ag-QRE) N4111(TFSI) became strongly attached to the Al surface, resulting in $dBE dE^{-1} \approx 0.1$ eV V⁻¹ and indicating the start of intense electro-oxidation processes at Al and finally the formation of Al(TFSI)₃. The EIS data, collected in the potentiostatic regime, show the formation of a series capacitance peaks and imaginary capacitance vs. potential curves at $E = 3.00$ V. CV data show that after activation of the Al electrode at $E = 3.00$ V (i.e., after the damage to the compact passivating Al₂O₃ layer), intensive Al electro-oxidation had started at $E \geq 1.10$ V (vs. Ag-QRE). Based on the in situ XPS $dBE dE^{-1}$ plots and CV data, it seems that Al protected by an Al₂O₃ layer (formed in dry air) as a current-collector material is (in general) electrochemically stable in the N4111(TFSI) environment up to ca. $E = 3.0$ V (vs. Ag-QRE). Thus, in situ XPS, potentiostatic EIS, and CV data are in an agreement with each other. It has been noted that at more positive potentials than $E = 6.5$ V (vs. Ag-QRE) a new intense oxidation process started at the Al electrode. The CV and in situ XPS data indicate that electro-oxidation of the TFSI⁻ anion takes place mainly at $E > 6.5$ V (vs. Ag-QRE), confirming its high electrochemical stability. When electro-oxidation of TFSI⁻ had taken place at the previously activated Al surface at $E \geq 6.5$ V, the products formed ensured the electrochemical stability of the N4111(TFSI)|Al interface only within a very narrow potential region—thus, only at $E < 1.1$ V (vs. Ag-QRE).

Supplementary Materials: The following supporting information can be downloaded at: <https://www.mdpi.com/article/10.3390/batteries9030189/s1>, Figure S1a–i: BE vs. E relationships for the elements forming butyltrimethylammonium bis(trifluoromethylsulfonyl)amide (N4111(TFSI)); Figure S2a–d: The cyclic voltammograms (CV) measured within the potential range from 0.00 V to the final potentials (indicated in the figures) and reverse at the potential sweep rate 1.00 mV s⁻¹. The

measured CVs are shown in various current scales; the second CV sweeps are presented; Figure S3a–d: The cyclic voltammograms (CV) measured within the potential range from 0.00 V to the final potentials (indicated in the figures) and reverse at the potential sweep rate 1.00 mV s^{-1} . The measured CVs are shown in various current scales; the second CV sweeps are presented; Figure S4: Nyquist plots measured for N4111(TFSI) | Al/Al₂O₃ system at $E = 7.00 \text{ V}$: pink—measured data, dark blue—fitted data, using equivalent circuit shown in Scheme 2a; Figure S5: Nyquist plots measured for N4111(TFSI) | Al/Al₂O₃ system at $E = 8.00 \text{ V}$: pink—measured data, dark blue—fitted data, using equivalent circuit shown in Scheme 2b; Figure S6: The complex power dependences for N4111(TFSI) | Al interface at various Al potentials applied.

Author Contributions: Conceptualization, J.K. and E.L.; Methodology, J.K., A.T. and T.K.; Formal Analysis, J.K. and T.K.; Investigation, J.K., T.K. and A.T.; Resources, A.T. and J.K.; Data Curation, J.K.; Writing—Original Draft Preparation, J.K.; Writing—Review & Editing, E.L. and K.L.; Project Administration, J.K.; Funding Acquisition, E.L. and V.K. All authors have read and agreed to the published version of the manuscript.

Funding: This work was supported by the EU through the European Regional Development Fund under projects TK 141 (2014-2020.4.01.15-0011), NAMUR+ (2014-2020.4.01.16-0123), and NAMUR (3.2.0304.12-0397); the Estonian Research Council (IUT20-57 and PRG676); the European Spallation Source: Estonian Participation in ESS Instrument design, development, and building and application for scientific research (SLOKT12026T and SLTKT16432T); the project “Production of Polymer Electrolyte Membrane Fuel Cell” (LLTKT20148); and the project “Developing new research services and research infrastructures at MAX IV synchrotron radiation source” (2014-2020.4.01.20-0278).

Institutional Review Board Statement: Not applicable.

Informed Consent Statement: Not applicable.

Data Availability Statement: Data sharing is not applicable to this article.

Acknowledgments: We acknowledge MAX IV Laboratory (University of Lund, Sweden) for the measurement time on Beamline FinEstBeAMS under Proposal 20210300. Research conducted at MAX IV, a Swedish-national user facility, is supported by the Swedish Research council under contract 2018-07152, the Swedish Governmental Agency for Innovation Systems under contract 2018-04969, and Formas under contract 2019-02496. We also acknowledge Beamline FinEstBeAMS Antti Kivimäki and Kirill Chernenko for their very kind support.

Conflicts of Interest: The authors declare no conflict of interest.

References

1. Lane, G.H. Electrochemical reduction mechanisms and stabilities of some cation types used in ionic liquids and other organic salts. *Electrochim. Acta* **2012**, *83*, 513–528. [[CrossRef](#)]
2. Mousavi, M.P.S.; Kashefolgheta, S.; Stein, A.; Bühlmann, P. Electrochemical Stability of Quaternary Ammonium Cations: An Experimental and Computational Study. *J. Electrochem. Soc.* **2016**, *163*, H74. [[CrossRef](#)]
3. Simon, P.; Gogotsi, Y. Materials for electrochemical capacitors. *Nat. Mater.* **2008**, *7*, 845–854. [[CrossRef](#)] [[PubMed](#)]
4. Peng, C.; Chang, L.; Zhang, Z.; Tachibana, K.; Yang, Y.; Zhao, S. Investigation of the anodic behaviour of Al current collector in room temperature ionic liquid electrolytes. *Electrochim. Acta* **2008**, *53*, 4764–4772. [[CrossRef](#)]
5. Ma, T.; Xu, G.-L.; Li, Y.; Wang, L.; He, X.; Zheng, J.; Liu, J.; Engelhard, M.H.; Zapol, P.; Curtiss, L.A.; et al. Revisiting the Corrosion of the Aluminium Current Collector in Lithium-Ion Batteries. *J. Phys. Chem. Lett.* **2017**, *8*, 1072–1077. [[CrossRef](#)]
6. Guo, L.; Thornton, D.B.; Koronfel, M.A.; Stephens, I.E.L.; Ryan, M.P. Degradation in lithium ion battery current collectors. *J. Phys. Energy* **2021**, *3*, 032015. [[CrossRef](#)]
7. Goldman, J.L.; McEwen, A.B. EMIM and EMIBet on Aluminum Anodic Stability Dependence on Lithium Salt and Propylene Carbonate. *Electrochem. Solid-State Lett.* **1999**, *2*, 501–503. [[CrossRef](#)]
8. Morita, M.; Shibata, T.; Yoshimoto, N.; Ishikawa, M. Anodic behavior of aluminum in organic solutions with different electrolytic salts for lithium ion batteries. *Electrochim. Acta* **2002**, *47*, 2787–2793. [[CrossRef](#)]
9. Cho, E.; Mun, J.; Chae, O.B.; Kwon, O.M.; Kim, H.-T.; Ryu, J.H.; Kim, Y.G.; Oh, S.M. Corrosion/passivation of aluminum current collector in bis(fluorosulfonyl)imide-based ionic liquid for lithium-ion batteries. *Electrochem. Commun.* **2012**, *22*, 1–3. [[CrossRef](#)]
10. Jänes, A.; Eskusson, J.; Kanarbik, R.; Saar, A.; Lust, E. Surface Analysis of Supercapacitor Electrodes After Long-Lasting Constant Current Tests in Organic Electrolyte. *J. Electrochem. Soc.* **2012**, *159*, A1141–A1147. [[CrossRef](#)]
11. Myung, S.-T.; Hitoshi, Y.; Sun, Y.-K. Electrochemical behavior and passivation of current collectors in lithium-ion batteries. *J. Mater. Chem.* **2011**, *21*, 9891–9911. [[CrossRef](#)]

12. Bessone, J.B.; Salinas, D.R.; Mayer, C.E.; Ebert, M.; Lorenz, W.J. An EIS study of aluminium barrier-type oxide films formed in different media. *Electrochim. Acta* **1992**, *37*, 2283–2290. [[CrossRef](#)]
13. Gudić, S.; Radošević, J.; Kliškić, M. Impedance and transient study of aluminium barrier-type oxide films. *J. Appl. Electrochem.* **1996**, *26*, 1027–1035. [[CrossRef](#)]
14. Tateishi, K.; Ogino, H.; Waki, A.; Ohishi, T.; Murakami, M.; Asoh, H.; Ono, S. Anodization Behavior of Aluminium in Ionic Liquids with Small Amount of Water. *Electrochemistry* **2013**, *81*, 440–447. [[CrossRef](#)]
15. Sokol, V.; Shulgov, V. Electrochemical Aluminium Oxide Technology for Production of Electronics. In Proceedings of the 2012 IEEE International Conference on Oxide Materials for Electronic Engineering (OMEE), Lviv, Ukraine, 3–7 September 2012; pp. 55–56. [[CrossRef](#)]
16. Ono, S. *Passive Films for Electrolytic Capacitors, Encyclopedia of Interfacial Chemistry*; Wandelt, K., Ed.; Elsevier: Amsterdam, The Netherlands, 2018; pp. 376–395. [[CrossRef](#)]
17. Braithwaite, J.W.; Gonzales, A.; Nagasubramanian, G.; Lucero, S.J.; Peebles, D.E.; Ohlhausen, J.A.; Cieslak, W.R. Corrosion of Lithium-Ion Battery Current Collectors. *J. Electrochem. Soc.* **1999**, *146*, 448–456. [[CrossRef](#)]
18. Bizot, C.; Blin, M.-A.; Guichard, P.; Hamon, J.; Fernandez, V.; Soudan, P.; Gaubicher, J.; Poizot, P. Aluminum current collector for high voltage Li-ion battery. Part I: A benchmark study with statistical analysis. *Electrochem. Commun.* **2021**, *126*, 107013. [[CrossRef](#)]
19. Bizot, C.; Blin, M.-A.; Guichard, P.; Soudan, P.; Gaubicher, J.; Poizot, P. Aluminum current collector for high voltage Li-ion battery. Part II: Benefit of the En⁺ Safe[®] primed current collector technology. *Electrochem. Commun.* **2021**, *126*, 107008. [[CrossRef](#)]
20. Shehata, O.S.; Abdel-karim, A.M.; Fatah, A.H.A. New Trends in Anodizing and Electrolytic Coloring of Metals. *Egypt. J. Chem.* **2022**, *65*, 229–241. [[CrossRef](#)]
21. Tsangaraki-Kaplanoglou, I.; Theohari, S.; Dimogerontakis, T.; Kallithrakas-Kontos, N.; Wang, Y.-M.; Kuo (Harry), H.-H.; Kia, S. An investigation of electrolytic coloring process of anodized aluminum coatings. *Surf. Coat. Technol.* **2006**, *201*, 2749–2759. [[CrossRef](#)]
22. Zhang, X.; Winget, B.; Doeff, M.; Evans, J.W.; Devine, T.M. Corrosion of Aluminium Current Collectors in Lithium-Ion Batteries with Electrolytes Containing LiPF₆. *J. Electrochem. Soc.* **2005**, *152*, B448–B454. [[CrossRef](#)]
23. Kühnel, R.-S.; Lübke, M.; Winter, M.; Passerini, S.; Balducci, A. Suppression of aluminum current collector corrosion in ionic liquid containing electrolytes. *J. Power Sources* **2012**, *214*, 178–184. [[CrossRef](#)]
24. Peng, C.; Yang, L.; Zhang, Z.; Tachibana, K.; Yang, Y. Anodic behavior of Al current collector in 1-alkyl-3-methylimidazolium bis[(trifluoromethyl)sulfonyl] amide ionic liquid electrolytes. *J. Power Sources* **2007**, *173*, 510–517. [[CrossRef](#)]
25. Zhang, X.; Devine, T.M. Identity of Passive Film Formed on Aluminium in Li-Ion Battery Electrolytes with LiPF₆. *J. Electrochem. Soc.* **2006**, *153*, B344–B351. [[CrossRef](#)]
26. Zhang, X.; Devine, T.M. Factors That Influence Formation of AlF₃ Passive Film on Aluminum in Li-Ion Battery Electrolytes with LiPF₆. *J. Electrochem. Soc.* **2006**, *153*, B375–B383. [[CrossRef](#)]
27. Balducci, A.; Dugas, R.; Taberna, P.L.; Simon, P.; Plée, D.; Mastragostino, M.; Passerini, S. High temperature carbon–carbon supercapacitor using ionic liquid as electrolyte. *J. Power Sources* **2007**, *165*, 922–927. [[CrossRef](#)]
28. Lin, R.; Taberna, P.L.; Fantini, S.; Presser, V.; Pérez, C.R.; Malbosc, F.; Rupesinghe, N.L.; Teo, K.B.K.; Kogotsi, Y.; Simon, P. Capacitive Energy Storage from –50 to 100 °C Using an Ionic Liquid Electrolyte. *J. Phys. Chem. Lett.* **2011**, *2*, 2396–2401. [[CrossRef](#)]
29. Hou, Y.; Li, R.; Liang, J. Simultaneous electropolishing and electrodeposition of aluminum in ionic liquid under ambient conditions. *Appl. Surf. Sci.* **2018**, *434*, 918–921. [[CrossRef](#)]
30. Hou, Y.; Li, R.; Liang, J.; Su, P.; Ju, P. Electropolishing of Al and Al alloys in AlCl₃/trimethylamine hydrochloride ionic liquid. *Surf. Coat. Technol.* **2018**, *335*, 72–79. [[CrossRef](#)]
31. Kityk, A.A.; Protsenko, V.S.; Danilov, F.I.; Kun, O.V.; Korniy, S.A. Electropolishing of aluminum in a deep eutectic solvent. *Surf. Coat. Technol.* **2019**, *375*, 143–149. [[CrossRef](#)]
32. Tõnisoo, A.; Kruusma, J.; Pärna, R.; Kikas, A.; Hirsimäki, M.; Nõmmiste, E.; Lust, E. In Situ XPS Studies of Electrochemically Negatively Polarized Molybdenum Carbide Derived Carbon Double Layer Capacitor Electrode. *J. Electrochem. Soc.* **2013**, *160*, A1084–A1093. [[CrossRef](#)]
33. Kruusma, J.; Tõnisoo, A.; Pärna, R.; Nõmmiste, E.; Lust, E. In Situ XPS Studies of Electrochemically Positively Polarized Molybdenum Carbide Derived Carbon Double Layer Capacitor Electrode. *J. Electrochem. Soc.* **2014**, *161*, A1266–A1277. [[CrossRef](#)]
34. Kooser, K.; Kivimäki, A.; Turunen, P.; Pärna, R.; Reisberg, L.; Kirm, M.; Valden, M.; Huttula, M.; Kukkk, E. Gas-phase endstation of electron, ion and coincidence spectroscopies for diluted samples at the FinEstBeAMS beamline of the MAX IV 1.5 GeV storage ring. *J. Synchrotron Rad.* **2020**, *27*, 1080–1091. [[CrossRef](#)] [[PubMed](#)]
35. Blundell, R.K.; Licence, P. Quaternary ammonium and phosphonium based ionic liquids: A comparison of common anions. *Phys. Chem. Chem. Phys.* **2014**, *16*, 15278–15288. [[CrossRef](#)] [[PubMed](#)]
36. Kruusma, J.; Käambre, T.; Tõnisoo, A.; Kisand, V.; Lust, K.; Lust, E. The electrochemical behaviour of butyltrimethylammonium bis(trifluoromethylsulfonyl)imide at negatively polarised aluminium electrode studied by in situ soft X-ray photoelectron spectroscopy, electrochemical impedance spectroscopy and cyclic voltammetry techniques. *J. Solid State Electrochem.* **2022**, *26*, 2805–2815. [[CrossRef](#)]
37. Hamm, U.W.; Lazarescu, V.; Kolb, D.M. Adsorption of pyrazine on Au(111) and Ag(111) electrodes an ex situ XPS study. *J. Chem. Soc. Faraday Trans.* **1996**, *92*, 3785–3790. [[CrossRef](#)]

38. Zhou, W.; Kolb, D.M. Influence of an electrostatic potential at the metal/electrolyte interface on the electron binding energy of adsorbates as probed by X-ray photoelectron spectroscopy. *Surf. Sci.* **2004**, *573*, 176–182. [[CrossRef](#)]
39. Konarov, A.; Kim, H.J.; Yashiro, H.; Myung, S.-T. Passivation of aluminum current collectors in non-aqueous carbonate solutions containing sodium or potassium hexafluorophosphate salts. *J. Mater. Chem. A* **2019**, *7*, 13012. [[CrossRef](#)]
40. Kühnel, R.-S.; Reiter, J.; Jeong, S.; Passerini, S.; Balducci, A. Anodic stability of aluminum current collectors in an ionic liquid based on the (fluorosulfonyl) (trifluoromethanesulfonyl)imide anion and its implication on high voltage supercapacitors. *Electrochem. Commun.* **2014**, *38*, 117–119. [[CrossRef](#)]
41. Kühnel, R.-S.; Balducci, A. Comparison of the anodic behavior of aluminum current collectors in imide-based ionic liquids and consequences on the stability of high voltage supercapacitors. *J. Power Sources* **2014**, *249*, 163–171. [[CrossRef](#)]
42. Brett, C.M.A. On the electrochemical behaviour of aluminium in acidic chloride solution. *Corr. Sci.* **1992**, *33*, 203–210. [[CrossRef](#)]
43. Jänes, A.; Thomberg, T.; Tõnurist, K.; Kurig, H.; Laheäär, A.; Lust, E. Micro- and Mesoporous Carbide-Derived Carbon Materials and Polymer Membranes for Supercapacitors. *ECS Transact.* **2008**, *16*, 57–67. [[CrossRef](#)]
44. Kurig, H.; Jänes, A.; Lust, E. Electrochemical Characteristics of Carbide-Derived Carbon | 1 -Ethyl-3-methylimidazolium Tetrafluoroborate Supercapacitor Cells. *J. Electrochem. Soc.* **2010**, *157*, A272–A279. [[CrossRef](#)]
45. Taberna, P.L.; Simon, P.; Fauvarque, J.F. Electrochemical Characteristics and Impedance Spectroscopy Studies of Carbon-Carbon Supercapacitors. *J. Electrochem. Soc.* **2003**, *150*, A292–A300. [[CrossRef](#)]
46. Harrington, D.A.; van der Driessche, P. Mechanism and equivalent circuits in electrochemical impedance spectroscopy. *Electrochim. Acta* **2011**, *56*, 8005–8013. [[CrossRef](#)]
47. Celsiulis, H.; Tsyntsaru, N.; Ramanavicius, A.; Ragoisha, G. The Study of Thin Films by Electrochemical Impedance Spectroscopy. In *Nanostructures and Thin Films for Multifunctional Applications, NanoScience and Technology*; Springer: Cham, Switzerland, 2016. [[CrossRef](#)]
48. Mann, R.; Nauer, G.E. A Mathematical Model for the Inductance Observed in the Impedance Spectrum of Corroding Aluminum. *ECS Transact.* **2009**, *19*, 1–12. [[CrossRef](#)]
49. Yang, C.; Li, C.Y.V.; Li, F.; Chan, K.-Y. Complex Impedance with Transmission Line Model and Complex Capacitance Analysis of Ion Transport and Accumulation in Hierarchical Core-Shell Porous Carbons. *J. Electrochem. Soc.* **2013**, *160*, H271–H278. [[CrossRef](#)]
50. Véliz, B.; Bermejo, S.; Orpella, A.; Castañer, L. Impedance modeling of silica nanoparticles metal insulator metal capacitors. *Electrochim. Acta* **2018**, *280*, 62–70. [[CrossRef](#)]
51. Costa, J.C.M.; Nascimento, M.C.; Silva, E.C.; Pereira, B.L.; Passos, R.R.; Pocrifka, L.A. Galvanostatic synthesis of MnO₂ in carbon cloth: An electrochemical impedance spectroscopy study. *J. Solid State Electrochem.* **2020**, *24*, 1727–1733. [[CrossRef](#)]
52. Costa, J.C.M.; Ferreira, C.S.; Silva, Y.F.; Cunha, M.R.; de Neto, J.C.M.; Giacon, V.M.; Passos, R.R.; Pocrifka, L.A. Electrochemical nanoarchitectonics and analysis of PMMA/NiO based on electrochemical impedance spectroscopy. *Mater. Sci. Eng. B* **2022**, *283*, 115833. [[CrossRef](#)]

Disclaimer/Publisher’s Note: The statements, opinions and data contained in all publications are solely those of the individual author(s) and contributor(s) and not of MDPI and/or the editor(s). MDPI and/or the editor(s) disclaim responsibility for any injury to people or property resulting from any ideas, methods, instructions or products referred to in the content.